



Homogenization assumptions for coupled multiscale analysis of structural elements: beam kinematics

Simon Klarmann¹ · Friedrich Gruttmann² · Sven Klinkel¹

Received: 4 June 2019 / Accepted: 4 October 2019 / Published online: 7 November 2019
© Springer-Verlag GmbH Germany, part of Springer Nature 2019

Abstract

This contribution proposes a multiscale scheme for structural elements considering beam kinematics. The scheme is based on a first-order homogenization approach fulfilling the Hill–Mandel condition. Within this paper, special focus is given to the transverse shear stiffness. Using basic boundary conditions, the transverse shear stiffness drastically depends on the size of the representative volume element (RVE). The reason for this size dependency is identified. As a consequence, additional internal constraints are proposed. With these new constraints, the homogenization scheme leads to cross-sectional values independent of the size of the RVE. As they are based on the beam assumptions, a homogeneous material distribution in the length direction yields optimal results. Furthermore, outcomes of the scheme are verified with simple linear elastic benchmark tests as well as nonlinear computations involving plasticity and cross-sectional deformations.

Keywords FE² · Homogenization · Beam · Structural element · Multiscale · Nonlinearity

1 Introduction

Beam elements provide a simple and efficient way to model large structures, provided the structure has a predominant direction. To exploit this geometrical property, highly simplified kinematical assumptions are made. As a result, the load-bearing behavior of a beam element is no longer characterized by the classical stresses and material parameters but is described with the help of stress resultants and their linearizations. This includes mainly tension, bending, torsion and shearing. If homogeneous structures with a strongly pronounced preferred direction are assumed, it is enough to consider tension and bending. Their corresponding cross-sectional parameters can be determined easily. If the beam to be considered becomes shorter, the shear deformation plays an increasingly important role. The determination of its corresponding stiffness is more complicated. A direct integration of the shear modulus over the cross-section leads to

an overestimation of the shear stiffness. To reduce this problem, shear correction factors are proposed, see e.g. [8,24]. Furthermore, higher-order shear deformation theories have been developed leading to refined beam formulations, see e.g. [21]. They include additional assumptions for the cross-sectional warping so that the shear stresses fulfill the stress boundary conditions. Another refined beam theory and its finite element application can be found in [2].

In addition to the shear stiffness, the torsional stiffness is also important. Both cases have in common that cross-sectional warping must be considered. As in the case of the higher-order shear deformation theories, the displacement field is enhanced by a warping function. Additionally, an associated degree of freedom is introduced to achieve the continuity of the displacement field throughout the cross-section, see e.g. [11,23]. As a result, additional stress resultants are introduced. Difficulties arise in determining the warping function or the corresponding cross-sectional parameters. However, this extension allows consideration of lateral torsional buckling.

Regarding the evaluation of the stiffness parameters, in [16,31] an asymptotic homogenization scheme is proposed. The scheme allows determination of necessary values for Timoshenko's beam theory. It can consider homogeneous as well as heterogeneous cross-sections and allows recovery of the 3D stress state. However, it is limited to

✉ Simon Klarmann
klarmann@lbb.rwth-aachen.de

¹ Lehrstuhl für Baustatik und Baudynamik, RWTH Aachen University, Mies-van-der-Rohe-Str. 1, 52074 Aachen, Germany

² Fachgebiet Festkörpermechanik, Technische Universität Darmstadt, Franziska-Braun-Str. 7, 64287 Darmstadt, Germany

linear elastic material behavior. In [1,3], this approach is extended to the homogenization of periodic structures using Bernoulli’s kinematical assumptions. An extension to shear-soft Timoshenko kinematics is presented in [30] with a focus on evaluating suitable shear correction factors. Leaving the linear regime, in [26,27] a coupled model to evaluate cross-sectional properties with consideration of the current stress–strain state is proposed.

Besides the previously mentioned works, numerical homogenization procedures have become popular in recent years. Based on them, the FE² method was developed, see e.g. [5,6]. It is often used to determine properties of yet unknown heterogeneous materials. The most interesting element of the approach is that the evaluation of a structure on macroscopic level and homogenization on a microscopic level are coupled. Therefore, physical nonlinear behavior on microscopic level can be considered. A comprehensive overview of the application of the FE² method can be found in [20]. Furthermore, it has already been used in conjunction with structural elements. In [4], for example, the Kirchhoff-Love shell theory is considered, and a second-order homogenization approach is used to carry out the multiscale computation. Within this shell theory, no transverse shear deformation is considered. It will be shown later that this deformation leads to problems when performing the homogenization. Despite this fact, a shear soft kinematic is considered in [7] by an extension of the previously mentioned second-order homogenization scheme. It is shown that the scheme can approximate the behavior of complex structures. Regarding the transverse shear deformation, possible boundary conditions are given. However, no linear elastic benchmark tests are performed, such as the evaluation of shear correction factors. Further contributions to performing a multiscale analysis with shell kinematics are [9,14]. In these papers, a first-order homogenization scheme is used. In [9], only the mesh convergence of the shear correction factor is investigated, while [14] also mentions that the evaluation of the transverse shear stiffness leads to problems. The latter also applies a shear correction factor based on the size of the representative volume element (RVE) that improves the results.

The current work proposes a multiscale scheme for beam structures, exhibiting the following properties:

- The macroscopic structure is modeled with Timoshenko beam elements. This means that the kinematical assumptions contain tension, bending and transverse shear deformations. This leads to a basic six degrees of freedom element that can incorporate geometrical nonlinearity; however, the strains are assumed to be small.
- The multiscale approach is based on a first-order homogenization scheme fulfilling the Hill–Mandel condition. This allows for the homogenization of 3D RVEs, which facilitates the modeling of general heterogeneous struc-

tures. This means that general 3D material laws can be used. Thus, physical nonlinearities can be considered. Furthermore, geometrical nonlinearity can be applied, since cross-sectional deformations may also be included.

- The reason for the dependency of the resulting shear stiffness on the size of the RVE is identified. Despite the basic boundary conditions, new internal constraints are proposed leading to results independent of the size of the RVE. With the new constraints, the numerical homogenization leads to well-known cross-sectional values for linear elastic benchmark tests, including shear correction factors.

2 Beam kinematics

The description of the beam kinematics is analogous to that in [27] by introducing the reference configuration Ω_0 at time $t = 0$ as well as the current configuration Ω_t at arbitrary time t in the Euclidean space \mathbf{e}_i . To describe an arbitrary point of the body, the local coordinate systems \mathbf{A}_i in the reference configuration and \mathbf{a}_i in the current configuration are introduced, see Fig. 1. The local coordinates are denoted as $\{\xi_1, \xi_2, \xi_3\}$. By introducing orthogonal tensors \mathbf{R}_0 and $\mathbf{R} \in SO(3)$, the relation between the coordinate systems can be expressed as

$$\mathbf{A}_i(S) = \mathbf{R}_0(S) \mathbf{e}_i, \mathbf{a}_i(S) = \mathbf{R}(S) \mathbf{e}_i \text{ with } \mathbf{R}_0, \mathbf{R} \in SO(3). \tag{1}$$

The parameter $S = \xi_1 \in [0, L]$ is the arclength of the spatial curve representing the beam. Therefore, the position vectors in the reference configuration \mathbf{X} and in the current configuration \mathbf{x} are

$$\begin{aligned} \mathbf{X}(S, \xi_2, \xi_3) &= \mathbf{X}_B(S) + \xi_2 \mathbf{A}_2(S) + \xi_3 \mathbf{A}_3(S), \\ \mathbf{x}(S, \xi_2, \xi_3, t) &= \mathbf{x}_B(S, t) + \xi_2 \mathbf{a}_2(S, t) + \xi_3 \mathbf{a}_3(S, t). \end{aligned} \tag{2}$$

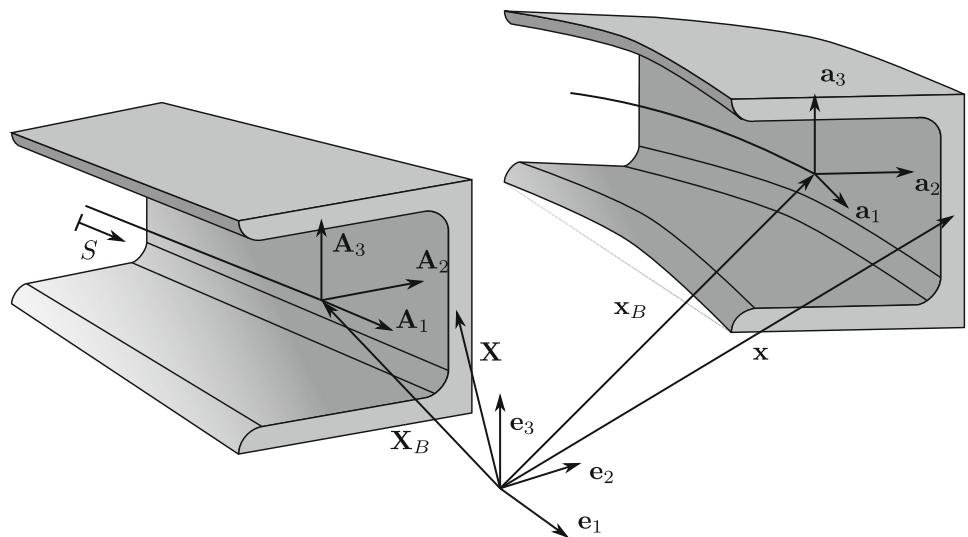
Using the position vectors Eq. (2), the tangent vectors are

$$\begin{aligned} \mathbf{G}_1 &= \mathbf{X}'_B + \xi_2 \mathbf{A}'_2 + \xi_3 \mathbf{A}'_3, & \mathbf{g}_1 &= \mathbf{x}'_B + \xi_2 \mathbf{a}'_2 + \xi_3 \mathbf{a}'_3, \\ \mathbf{G}_2 &= \mathbf{A}_2, & \mathbf{g}_2 &= \mathbf{a}_2, \\ \mathbf{G}_3 &= \mathbf{A}_3, & \mathbf{g}_3 &= \mathbf{a}_3. \end{aligned} \tag{3}$$

The notation $\{\bullet\}'$ indicates the derivative with respect to the arclength S . Considering $\mathbf{R}_0 = \mathbf{A}_i \otimes \mathbf{e}_i$ and $\mathbf{R} = \mathbf{a}_i \otimes \mathbf{e}_i$, the pull-back of the covariant basis systems can be defined. This leads to the vectors

$$\begin{aligned} \mathbf{F}_1 &= \mathbf{R}_0^T \mathbf{G}_1 = \bar{\mathbf{e}}_0 + \mathbf{e}_1 + \bar{\kappa}_0 \times \mathbf{d}, & \mathbf{f}_1 &= \mathbf{R}^T \mathbf{g}_1 = \bar{\mathbf{e}}_t + \mathbf{e}_1 + \bar{\kappa}_t \times \mathbf{d}, \\ \mathbf{F}_2 &= \mathbf{R}_0^T \mathbf{G}_2 = \mathbf{e}_2, & \mathbf{f}_2 &= \mathbf{R}^T \mathbf{g}_2 = \mathbf{e}_2, \\ \mathbf{F}_3 &= \mathbf{R}_0^T \mathbf{G}_3 = \mathbf{e}_3, & \mathbf{f}_3 &= \mathbf{R}^T \mathbf{g}_3 = \mathbf{e}_3 \end{aligned} \tag{4}$$

Fig. 1 Kinematical assumptions



with $\mathbf{d} = \xi_2 \mathbf{e}_2 + \xi_3 \mathbf{e}_3$. Using Eq. (4), the relation to the beam strains $\bar{\boldsymbol{\varepsilon}}_0, \bar{\boldsymbol{\kappa}}_0$ and $\bar{\boldsymbol{\varepsilon}}_t, \bar{\boldsymbol{\kappa}}_t$ is established. Therefore, the vector \mathbf{F}_1 can be expressed as

$$\mathbf{F}_1 = \begin{bmatrix} 1 & 0 & 0 & 0 & \xi_3 & -\xi_2 \\ 0 & 1 & 0 & -\xi_3 & 0 & 0 \\ 0 & 0 & 1 & \xi_2 & 0 & 0 \end{bmatrix} \begin{bmatrix} \bar{\boldsymbol{\varepsilon}} \\ \bar{\boldsymbol{\kappa}} \end{bmatrix}_0 + \begin{bmatrix} 1 \\ 0 \\ 0 \end{bmatrix} = \mathbf{A} \begin{bmatrix} \bar{\boldsymbol{\varepsilon}} \\ \bar{\boldsymbol{\kappa}} \end{bmatrix}_0 + \mathbf{e}_1 = \mathbf{A} \boldsymbol{\varepsilon}_0 + \mathbf{e}_1. \tag{5}$$

Furthermore, rewriting \mathbf{f}_1 using Eq. (5) and replacing $\boldsymbol{\varepsilon}_0$ with $\boldsymbol{\varepsilon}_t$, leads to

$$\mathbf{f}_1 = \mathbf{A} \boldsymbol{\varepsilon}_t + \mathbf{e}_1. \tag{6}$$

Using the definition of the Green–Lagrange strains in a convective coordinate system,

$$\mathbf{E} = \frac{1}{2} (g_{ij} - G_{ij}), \tag{7}$$

with the metric tensors $g_{ij} = \mathbf{g}_i \cdot \mathbf{g}_j$ and $G_{ij} = \mathbf{G}_i \cdot \mathbf{G}_j$ as well as the fact that $\mathbf{R}_0 \mathbf{R}_0^T = \mathbf{R} \mathbf{R}^T = \mathbf{1}$, leads to

$$\mathbf{E} = \frac{1}{2} (\mathbf{f}_i \cdot \mathbf{f}_j - \mathbf{F}_i \cdot \mathbf{F}_j). \tag{8}$$

The non-vanishing terms due to the kinematical assumptions read

$$\mathbf{E}_B = \begin{bmatrix} E_{11} \\ 2E_{12} \\ 2E_{13} \end{bmatrix} = \begin{bmatrix} \frac{1}{2} (\mathbf{f}_1 \cdot \mathbf{f}_1 - \mathbf{F}_1 \cdot \mathbf{F}_1) \\ \mathbf{f}_1 \cdot \mathbf{f}_2 - \mathbf{F}_1 \cdot \mathbf{F}_2 \\ \mathbf{f}_1 \cdot \mathbf{f}_3 - \mathbf{F}_1 \cdot \mathbf{F}_3 \end{bmatrix} = \begin{bmatrix} \frac{1}{2} (2\mathbf{A} (\boldsymbol{\varepsilon}_t - \boldsymbol{\varepsilon}_0) \cdot \mathbf{e}_1 + \boldsymbol{\varepsilon}_t \cdot \mathbf{A}^T \mathbf{A} \boldsymbol{\varepsilon}_t - \boldsymbol{\varepsilon}_0 \cdot \mathbf{A}^T \mathbf{A} \boldsymbol{\varepsilon}_0) \\ \mathbf{A} (\boldsymbol{\varepsilon}_t - \boldsymbol{\varepsilon}_0) \cdot \mathbf{e}_2 \\ \mathbf{A} (\boldsymbol{\varepsilon}_t - \boldsymbol{\varepsilon}_0) \cdot \mathbf{e}_3 \end{bmatrix}. \tag{9}$$

The terms in Eq. (9) contain the beam strains $\boldsymbol{\varepsilon}_0$, which represent the initial distortion in the reference configuration, as well as $\boldsymbol{\varepsilon}_t$, which represents the distortion in the current configuration. In this contribution small strains are assumed, hence $\boldsymbol{\varepsilon}_t \cdot \mathbf{A}^T \mathbf{A} \boldsymbol{\varepsilon}_t - \boldsymbol{\varepsilon}_0 \cdot \mathbf{A}^T \mathbf{A} \boldsymbol{\varepsilon}_0 \approx \mathbf{0}$ leads to

$$\mathbf{E}_B = \mathbf{A} (\boldsymbol{\varepsilon}_t - \boldsymbol{\varepsilon}_0) = \mathbf{A} \begin{bmatrix} \bar{\boldsymbol{\varepsilon}}_t - \bar{\boldsymbol{\varepsilon}}_0 \\ \bar{\boldsymbol{\kappa}}_t - \bar{\boldsymbol{\kappa}}_0 \end{bmatrix} = \mathbf{A} \begin{bmatrix} \bar{\boldsymbol{\varepsilon}} \\ \bar{\boldsymbol{\kappa}} \end{bmatrix} = \mathbf{A} \boldsymbol{\varepsilon}, \tag{10}$$

which main impact lies in the application of the RVE boundary conditions. Therefore, the Green–Lagrange strains Eq. (10) are expressed via the difference of the beam strains in the current configuration $\boldsymbol{\varepsilon}_t$ minus the beam strains in the reference configuration $\boldsymbol{\varepsilon}_0$. Those strains can be split into the normal and shear strain vector $\bar{\boldsymbol{\varepsilon}}$ and the curvature part $\bar{\boldsymbol{\kappa}}$. For the final stress-generating strains, the indices t and 0 are dropped. The derivatives of the orthonormal basis system can be expressed as $\mathbf{A}'_i = \boldsymbol{\theta}_0 \times \mathbf{A}_i$ and $\mathbf{a}'_i = \boldsymbol{\theta}_t \times \mathbf{a}_i$ by introducing the axial vectors $\boldsymbol{\theta}_0$ and $\boldsymbol{\theta}_t$. Finally, the strain vectors are defined as

$$\bar{\boldsymbol{\varepsilon}}_t + \mathbf{e}_1 = \mathbf{R}^T \mathbf{x}'_B = \begin{bmatrix} \mathbf{x}'_B \cdot \mathbf{a}_1 \\ \mathbf{x}'_B \cdot \mathbf{a}_2 \\ \mathbf{x}'_B \cdot \mathbf{a}_3 \end{bmatrix}, \quad \boldsymbol{\kappa}_t = \mathbf{R}^T \boldsymbol{\theta} = \begin{bmatrix} \mathbf{a}'_2 \cdot \mathbf{a}_3 \\ \mathbf{a}'_3 \cdot \mathbf{a}_1 \\ \mathbf{a}'_1 \cdot \mathbf{a}_2 \end{bmatrix}. \tag{11}$$

Analogous to Eq. (11), the strain vectors in the reference configuration read $\boldsymbol{\varepsilon}_0 + \mathbf{e}_1 = \mathbf{R}_0^T \mathbf{X}'_0$ and $\boldsymbol{\kappa}_0 = \mathbf{R}_0^T \boldsymbol{\theta}_0$. Accordingly, the variations of the Green–Lagrange strains can be expressed as

$$\delta \mathbf{E}_B = \mathbf{A} \delta (\boldsymbol{\varepsilon}_t - \boldsymbol{\varepsilon}_0) = \mathbf{A} \begin{bmatrix} \delta \bar{\boldsymbol{\varepsilon}}_t \\ \delta \bar{\boldsymbol{\kappa}}_t \end{bmatrix} = \mathbf{A} \begin{bmatrix} \delta \bar{\boldsymbol{\varepsilon}} \\ \delta \bar{\boldsymbol{\kappa}} \end{bmatrix} = \mathbf{A} \delta \boldsymbol{\varepsilon}. \tag{12}$$

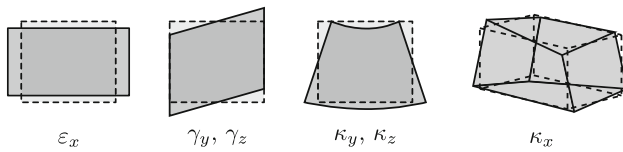


Fig. 2 Deformations of an infinitesimal beam element

Thus, the essential parts of the kinematics are described, whereby individual components of beam distortions can be represented according to Fig. 2, provided that an originally straight and untwisted beam is assumed. The particular components are $\bar{\boldsymbol{\varepsilon}} = [\varepsilon_x, \gamma_y, \gamma_z]$ and $\bar{\boldsymbol{\kappa}} = [\kappa_x, \kappa_y, \kappa_z]$.

To obtain an expression for the corresponding internal forces, it is sufficient to insert the first variations of the Green–Lagrange strains into the generally known, weak form of equilibrium

$$g(\delta \mathbf{u}, \mathbf{u}) = \int_{\Omega_0} \delta \mathbf{E} : \mathbf{S} dV + \int_{\Omega_0} \delta \mathbf{u} \cdot \mathbf{f} dV + \int_{\partial \Omega_{\sigma 0}} \delta \mathbf{u} \cdot \bar{\mathbf{t}} dA = 0. \quad (13)$$

In Eq. (13), $\mathbf{u} = [u_x, u_y, u_z]$ is the displacement field and $\delta \mathbf{u}$ the corresponding variation. Accordingly, \mathbf{S} is the 2. Piola–Kirchhoff stress tensor, which is work conforming to the Green–Lagrange strain tensor. The vector \mathbf{f} contains the volume loads and $\bar{\mathbf{t}}$ the applied boundary loads. To evaluate the equations, the integration is performed over the reference configuration Ω_0 and its stress boundary $\partial \Omega_{\sigma 0}$. In this contribution, the virtual internal work $\int_{\Omega_0} \delta \mathbf{E} : \mathbf{S} dV$ is of particular interest.

Inserting the variation of the Green–Lagrange strains Eq. (12) into the weak form of equilibrium Eq. (13) and reducing the 2. Piola–Kirchhoff stresses to the non-vanishing terms $\mathbf{S}_B = [S^{11}, S^{12}, S^{13}]^T$, the virtual internal work then reads

$$\int_{\Omega_0} \delta \mathbf{E} : \mathbf{S} dV = \int_{\Omega_0} \delta \mathbf{E}_B \cdot \mathbf{S}_B dV = \int_{\Omega_0} \mathbf{A} \delta \boldsymbol{\varepsilon} \cdot \mathbf{S}_B dV. \quad (14)$$

The integration of Eq. (14) can now be split into an integration along the beam’s length and an integration over its cross-section. This leads to

$$\int_{\Omega_0} \mathbf{A} \delta \boldsymbol{\varepsilon} \cdot \mathbf{S}_B dV = \int_L \delta \boldsymbol{\varepsilon} \cdot \int_A \mathbf{A}^T \mathbf{S}_B dA dS. \quad (15)$$

With Eq. (15), the definition of the beam stress resultants can be derived as

$$\int_A \mathbf{A}^T \mathbf{S}_B dA = \int_A \begin{bmatrix} S^{11} \\ S^{12} \\ S^{13} \\ S^{13} \xi_2 - S^{12} \xi_3 \\ S^{11} \xi_3 \\ -S^{11} \xi_2 \end{bmatrix} dA = \begin{bmatrix} \mathbf{F} \\ \mathbf{M} \end{bmatrix} = \boldsymbol{\sigma}. \quad (16)$$

The stress resultants Eq. (16) contain the three forces $\mathbf{F} = [N, Q^2, Q^3]$ as well as the three moments $\mathbf{M} = [M^1, M^2, M^3]$. Herein, N denotes the normal force, Q^2, Q^3 the shear forces, M^1 the torsional moment and M^2, M^3 the bending moments. The linearization of Eq. (16) finally leads to

$$\int_A \mathbf{A}^T \mathbf{C} \Delta \mathbf{E}_B dA = \int_A \mathbf{A}^T \mathbf{C} \mathbf{A} \Delta \boldsymbol{\varepsilon} dA = \int_A \underbrace{\mathbf{A}^T \mathbf{C} \mathbf{A} dA}_{\mathbf{D}} \Delta \boldsymbol{\varepsilon}, \quad (17)$$

in which \mathbf{C} is the material tangent in continuum mechanics theory. With Eqs. (16) and (17), the main parts of the beam theory for this contribution are derived. It is well-known that the direct integration overestimates the stiffness of the beam. The main reason is the suppressed warping of the cross-section with the result that shear stresses do not fulfill the stress boundary conditions. This affects the torsional as well as the shear stiffnesses of the beam. Under the assumption of linear elasticity, an improved version of the material tangent is derived in [26] by considering higher order strains that represent the cross-sectional warping. This matrix reads

$$\mathbf{D} = \begin{bmatrix} EA & 0 & 0 & 0 & EA s_3 & -EA s_2 \\ GA_{S2} & 0 & -GA_{S2} m_3 & 0 & 0 & 0 \\ & GA_{S3} & GA_{S3} m_2 & 0 & 0 & 0 \\ & & GI_T & 0 & 0 & 0 \\ sym. & & & EI_2 & EI_{23} & \\ & & & & & EI_3 \end{bmatrix}. \quad (18)$$

The linearized stress resultants given in Eq. (18) will be used as a reference solution to benchmark the proposed homogenization scheme. The values contained in Eq. (18) are the tension stiffness EA , the two effective shear stiffnesses GA_{S2} and GA_{S3} , the torsional stiffness GI_T , the bending stiffnesses EI_2 and EI_3 , and the deviatoric part EI_{23} . Additionally, the matrix contains terms due to eccentricities given by the distances s_2 and s_3 of the center of gravity C to the beam reference line and the distances m_2, m_3 from the center of shear M to the beam reference line, see Fig. 3. To evaluate the torsion constant $I_T = I_T^* + A_{S2} \cdot m_3^2 + A_{S3} \cdot m_2^2$, the torsion constant I_T^* with respect to the center of shear as well

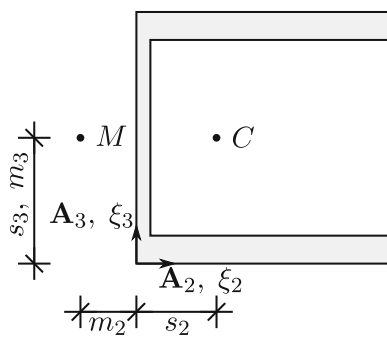


Fig. 3 General geometry of a cross-section

as the effective shear areas A_{S2} , A_{S3} and the distances m_2 , m_3 enter. Regarding the beam theory all relevant parts for this contribution are described. The derivation of the finite element equations of the beam element can be found in the literature, e.g. [11,23,27]. Regarding the evaluation of the examples, it should be mentioned that a pure displacement formulation with a reduced order integration is used.

3 Homogenization

In this work, homogenization is based on the first-order theory of Hill–Mandel [15]. Therefore, an RVE is introduced that represents the microscopic scale. It is required that the volume-averaged virtual internal work on the microscopic scale equals the virtual internal work of the corresponding macroscopic point

$$\langle \mathbf{P}^m : \delta \mathbf{F}^m \rangle - \mathbf{P}^M : \delta \mathbf{F}^M = 0. \tag{19}$$

In Eq. (19) \mathbf{P} is the first Piola–Kirchhoff stress tensor, which is work conforming to the deformation gradient \mathbf{F} . Furthermore, values on the microscopic scale are denoted with $\{\bullet\}^m$ and those on the macroscopic scale with $\{\bullet\}^M$. The brackets $\langle \bullet \rangle = \frac{1}{V_m} \int_{V_m} \{\bullet\} dV$ indicate volume average over the microscopic body. To identify suitable boundary conditions, Eq. (19) can be reformulated as a surface integral

$$\langle \mathbf{P}^m : \delta \mathbf{F}^m \rangle - \mathbf{P}^M : \delta \mathbf{F}^M = \frac{1}{V_m} \int_{A^m} (\delta \mathbf{x}^m - \delta \mathbf{F}^M \mathbf{X}^m) \cdot (\mathbf{t}_0^m - \mathbf{P}^M \mathbf{N}) dA, \tag{20}$$

see e. g. [20,22], where the vectors \mathbf{X}^m and \mathbf{x}^m represent position vectors in the reference and current configuration of the microscopic scale. The stress vector is denoted as \mathbf{t}_0^m , and the corresponding normal vector of the surface is called \mathbf{N} , both with respect to the reference configuration. Integration is performed over the surface A^m on the microscopic scale. In this work, essential boundary conditions that fulfill Eq. (20)

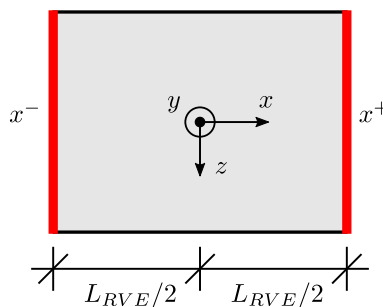


Fig. 4 Definition of the RVE in the case of the assumed beam kinematics

are periodic boundary conditions

$$\mathbf{x}^{m+} - \mathbf{x}^{m-} = \mathbf{F}^M \mathbf{X}^{m+} - \mathbf{F}^M \mathbf{X}^{m-} \tag{21}$$

and displacement boundary conditions

$$\mathbf{x}^m = \mathbf{F}^M \mathbf{X}^m. \tag{22}$$

The latter will be used for comparison reasons only. It should be noted that up to now the term “microscopic” has been used, but the term “mesoscopic” is more appropriate when transferring to beam systems. Therefore, this term will be used in what follows.

3.1 Beam kinematics

In the case of beam kinematics, there are two problems that arise when using periodic boundary conditions according to Eq. (21). On the one hand, a shear deformation of the RVE leads to a rigid body rotation only; on the other hand, the homogenized shear stiffness depends on the length of the RVE and shows no convergent behavior. Furthermore, the length dependency also affects the displacement boundary conditions. This work introduces additional constraints to eliminate these problems. To address these problems, a definition of the RVE which allows for application of the beam strains is first needed. Then it will be shown that under those assumptions, the Hill–Mandel condition is fulfilled, and the homogenization scheme leads to the definition of the beam stress resultants.

The assumed RVE with boundary conditions is depicted in Fig. 4, which shows a side view of it. Here, it is assumed that the RVE is modeled in an orthonormal basis system x , y , z , with the x -axis representing the beam axis. Therefore, the RVE extends in the x -direction from $-L_{RVE}/2$ to $L_{RVE}/2$, with L_{RVE} as the length of the RVE. The cross-section of the beam is modeled in the y , z -plane, but neither its center of gravity nor its center of shear necessarily lies on the x -axis. Thus, a general eccentricity can be considered. To deform the RVE according to the beam kinematics, the strains are

imposed on the positive x^+ and negative x^- side of the RVE according to Eq. (21) or Eq. (22). Furthermore, it is assumed that the remaining surfaces of the RVE are stress free. Finally, the only element missing in terms of the beam kinematics is the deformation gradient \mathbf{F}^M . Under the assumption of an initially straight and untwisted beam it can be expressed as $\mathbf{F} = [\mathbf{f}_1 \ \mathbf{f}_2 \ \mathbf{f}_3]$, with \mathbf{f}_1 , \mathbf{f}_2 and \mathbf{f}_3 according to Eq. (4). This leads to

$$\mathbf{F}^M - \mathbf{1} = \begin{bmatrix} \varepsilon_x + \kappa_y \cdot z - \kappa_z \cdot y & 0 & 0 \\ \gamma_y - \kappa_x \cdot z & 0 & 0 \\ \gamma_z + \kappa_x \cdot y & 0 & 0 \end{bmatrix}. \tag{23}$$

As this description results from the beam theory according to Sect. 2, it is considered as a consistent description. The corresponding deformations are depicted in Fig. 2. Another possibility is to subject the shear deformation to a rigid body rotation [29]. This leads to the slightly different definition of the deformation gradient

$$\mathbf{F}^M - \mathbf{1} = \begin{bmatrix} \varepsilon_x + \kappa_y \cdot z - \kappa_z \cdot y & \gamma_y & \gamma_z \\ -\kappa_x \cdot z & 0 & 0 \\ \kappa_x \cdot y & 0 & 0 \end{bmatrix}. \tag{24}$$

For the numerical implementation, the definition according to Eq. (23) is used, while the version according to Eq. (24) is used to show the problem of the rigid body rotation when applying a shear deformation with periodic boundary conditions. To check whether the Hill–Mandel condition is fulfilled, those equations need to be inserted into Eq. (19). As the cross-sectional information needs to be preserved, the homogenization, or “volume averaging,” is performed only over the length of the RVE, meaning that $\langle \bullet \rangle = 1/L_{RVE} \int_{\Omega_0^m} \{ \bullet \} \, dV$. As a result, a reformulation of Eq. (19) leads to

$$\delta \boldsymbol{\varepsilon} \cdot \boldsymbol{\sigma} = \frac{1}{L_{RVE}} \int_{\partial \Omega_0^m} \delta \mathbf{x}^m \cdot \mathbf{P}^m \mathbf{N} \, dA. \tag{25}$$

Inserting the definition of the deformation gradient in the form of Eq. (23) or Eq. (24) into Eq. (25) must lead to the definition of the stress resultants. As can be seen, only a surface integration over $\partial \Omega_0^m$ is necessary to derive the stress resultants. For simplification, and to be consistent with the beam theory of Sect. 2, small deformations are assumed. This means that $\mathbf{F} \approx \mathbf{1}$ and $\mathbf{P} = \mathbf{F}\mathbf{S} \approx \mathbf{S}$. Furthermore, the RVE is introduced in such a way that the normal vectors $\mathbf{N}^+ = -\mathbf{N}^- = [1, 0, 0]^T$ of the surfaces with boundary conditions are parallel to the x -axis and pointing in opposite directions on opposite faces. What remains for the mesoscopic stress state in the integral is $\mathbf{P}\mathbf{N} \approx \mathbf{S}\mathbf{N} = \pm [S^{11}, S^{12}, S^{13}]^T$.

Inserting this stress vector into Eq. (25) leads to

$$\delta \boldsymbol{\varepsilon} \cdot \boldsymbol{\sigma} = \frac{1}{L_{RVE}} \left\{ \int_{\partial \Omega_0^{m+}} \delta \mathbf{x}^{m+} \cdot \begin{bmatrix} S^{11} \\ S^{12} \\ S^{13} \end{bmatrix}^+ \, dA - \int_{\partial \Omega_0^{m-}} \delta \mathbf{x}^{m-} \cdot \begin{bmatrix} S^{11} \\ S^{12} \\ S^{13} \end{bmatrix}^- \, dA \right\}. \tag{26}$$

Finally, the expressions for the displacement as well as the periodic boundary conditions can be derived by inserting Eqs. (23) and (24) into Eqs. (21) and (22). To proceed, the variations are needed which can be expressed as

$$\begin{aligned} \delta \mathbf{x}^{m+} - \delta \mathbf{x}^{m-} &= \delta \mathbf{F}^M \mathbf{X}^{m+} - \delta \mathbf{F}^M \mathbf{X}^{m-} \\ &= \delta \mathbf{F}^M (\mathbf{X}^{m+} - \mathbf{X}^{m-}) = \delta \mathbf{F}^M \Delta \mathbf{X} \end{aligned} \tag{27}$$

for periodic boundary conditions and

$$\delta \mathbf{x} = \delta \mathbf{F}^M \mathbf{X} \tag{28}$$

for displacement boundary conditions. As the main goal is to derive periodic boundary conditions that allow cross-sectional warping, it is natural to assume that the faces on the x^+ and x^- side of the RVE are geometrically identical. First, using Eq. (28) with the relation according to Eq. (24) and inserting it into Eq. (26) leads to

$$\delta \boldsymbol{\varepsilon} \cdot \boldsymbol{\sigma} = \frac{1}{L_{RVE}} \delta \boldsymbol{\varepsilon} \cdot \int_{\partial \Omega_0^{m+}} \begin{bmatrix} S^{11} \hat{x} \\ S^{11} \hat{y} \\ S^{11} \hat{z} \\ -S^{12} \hat{x}z + S^{13} \hat{x}y \\ S^{11} \hat{x}z \\ -S^{11} \hat{x}y \end{bmatrix}^+ - \begin{bmatrix} S^{11} \hat{x} \\ S^{11} \hat{y} \\ S^{11} \hat{z} \\ -S^{12} \hat{x}z + S^{13} \hat{x}y \\ S^{11} \hat{x}z \\ -S^{11} \hat{x}y \end{bmatrix}^- \, dA. \tag{29}$$

To distinguish between the positions contained in \mathbf{F} and \mathbf{X} , the latter are expressed with $\mathbf{X} = [\hat{x}, \hat{y}, \hat{z}]^T$. Furthermore, it is assumed that the cross-sections at x^- and x^+ are identical. Therefore, the integration over the surface can be carried out on either side, e.g., over $\partial \Omega_0^+$ as in Eq. (29). The values that need to be considered for x^+ and x^- are identified by the brackets $[\bullet]^+$ and $[\bullet]^-$, respectively. Performing the

integration over the area leads to

$$\delta \boldsymbol{\varepsilon} \cdot \boldsymbol{\sigma} = \frac{1}{2} \delta \boldsymbol{\varepsilon} \cdot \left(\begin{bmatrix} N \\ \frac{-1}{L_{RVE}} M^z \\ \frac{1}{L_{RVE}} M^y \\ M^x \\ M^y \\ M^z \end{bmatrix}^+ + \begin{bmatrix} N \\ \frac{1}{L_{RVE}} M^z \\ \frac{-1}{L_{RVE}} M^y \\ M^x \\ M^y \\ M^z \end{bmatrix}^- \right). \quad (30)$$

The assumed relationships between displacements and beam strains according to Eq. (24) reveal the first problem that arises when using the homogenization scheme with the beam kinematics in Eq. (30). While the results for the normal force and the moments clearly lead to the correct values, the shear forces can only be recovered due to the equilibrium state. This means $\frac{dM^y}{dx} = Q^z$ and $\frac{dM^z}{dx} = -Q^y$. Collecting the terms finally leads to

$$\delta \boldsymbol{\varepsilon} \cdot \boldsymbol{\sigma} = \delta \boldsymbol{\varepsilon} \cdot \begin{bmatrix} N \\ \frac{-\Delta M^z}{L_{RVE}} \\ \frac{\Delta M^y}{L_{RVE}} \\ M^x \\ M^y \\ M^z \end{bmatrix} = \delta \boldsymbol{\varepsilon} \cdot \begin{bmatrix} N \\ Q^y \\ Q^z \\ M^x \\ M^y \\ M^z \end{bmatrix} \quad (31)$$

Evaluation of Eq. (29) with the result according to Eq. (31) is only valid for the displacement boundary conditions. If periodic boundary conditions are assumed, anti-periodic tractions must be considered. This means $[S^{11} \ S^{12} \ S^{13}]^+ = [S^{11} \ S^{12} \ S^{13}]^-$, and therefore, Eq. (29) evaluates to

$$\delta \boldsymbol{\varepsilon} \cdot \boldsymbol{\sigma} = \delta \boldsymbol{\varepsilon} \cdot \begin{bmatrix} N \\ 0 \\ 0 \\ M^x \\ M^y \\ M^z \end{bmatrix} = \delta \boldsymbol{\varepsilon} \cdot \begin{bmatrix} N \\ 0 \\ 0 \\ M^x \\ M^y \\ M^z \end{bmatrix}. \quad (32)$$

As can be seen, the periodic boundary conditions do not yield any result for the shear forces. Consequently, the resulting shear stiffness will be zero in the case of pure periodic boundary conditions.

On the other hand, using the consistent description according to Eq. (23) and inserting it into Eq. (26) yields

$$\delta \boldsymbol{\varepsilon} \cdot \boldsymbol{\sigma} = \frac{1}{L_{RVE}} \delta \boldsymbol{\varepsilon} \cdot \int_{\partial \Omega_0^{m+}} \hat{\boldsymbol{x}}^+ \begin{bmatrix} S^{11} \\ S^{12} \\ S^{13} \\ -S^{12}_z + S^{13}_y \\ S^{11}_z \\ -S^{11}_y \end{bmatrix}^+ dA$$

$$- \hat{\boldsymbol{x}}^- \begin{bmatrix} S^{11} \\ S^{12} \\ S^{13} \\ -S^{12}_z + S^{13}_y \\ S^{11}_z \\ -S^{11}_y \end{bmatrix}^- dA. \quad (33)$$

Evaluating Eq. (33) for both the periodic and the displacement boundary conditions results in

$$\delta \boldsymbol{\varepsilon} \cdot \boldsymbol{\sigma} = \frac{1}{2} \delta \boldsymbol{\varepsilon} \cdot \left(\begin{bmatrix} N \\ Q^y \\ Q^z \\ M^x \\ M^y \\ M^z \end{bmatrix}^+ + \begin{bmatrix} N \\ Q^y \\ Q^z \\ M^x \\ M^y \\ M^z \end{bmatrix}^- \right) = \delta \boldsymbol{\varepsilon} \cdot \begin{bmatrix} N \\ Q^y \\ Q^z \\ M^x \\ M^y \\ M^z \end{bmatrix}. \quad (34)$$

Comparing Eqs. (33) and (34) with Eq. (16) shows that the homogenization scheme yields consistent definitions of the stress resultants. But, regarding the final interpretation, the results of both relations between the displacements on the mesoscopic scale and the macroscopic stress, Eqs. (24) and (23) need to be considered. The only difference between Eqs. (23) and (24) is a rigid body rotation regarding the shear deformation. Therefore, even though Eq. (34) yields the consistent definition of the stress resultants, the RVE performs a rigid body rotation if a shear deformation is applied using periodic boundary conditions. In this case the resulting shear stresses S^{12} and S^{13} are zero. Additionally, looking at Eq. (31), the equilibrium state of the RVE needs to be considered, as the constant shear force introduces a linear moment distribution. Thus, the remaining tasks are:

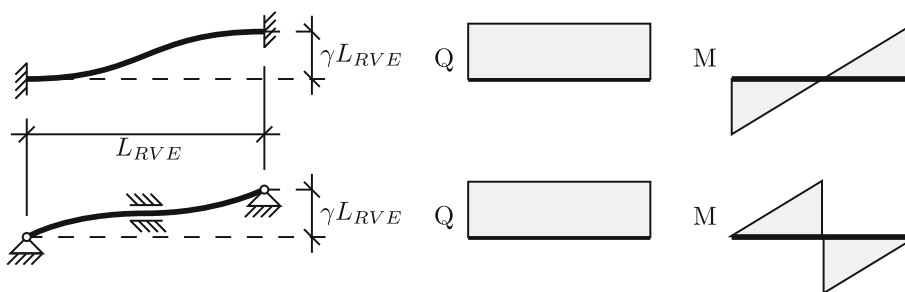
- Remove the rigid body rotations, provided that a shear deformation with the periodic boundary conditions is applied.
- Interpret the equilibrium state caused by a shear deformation.

While the rigid body rotation affects only the periodic boundary conditions, the equilibrium state needs to be considered for both boundary conditions.

3.2 Equilibrium state due to a shear deformation

As is evident from Eq. (31), a shear deformation of the RVE does not result in a pure shear stress state but also causes a linear moment distribution over its length. The associated differential relations between the shear force and the moment

Fig. 5 RVE subjected to a shear deformation according to Eq. (23), including stress resultants – upper: RVE displacement boundary conditions, lower: RVE with periodic boundary conditions and rigid body rotation constraint in the center



in the case of beam stress resultants read

$$-\frac{dM^z}{dx} = Q^y \quad \text{and} \quad \frac{dM^y}{dx} = Q^z. \tag{35}$$

Constructing an equivalent beam system for the RVE with respect to the chosen boundary conditions, the equilibrium state according to Eq. (35) can be evaluated.

In the case of the displacement boundary conditions, the equivalent beam system representing the RVE under a shear deformation γ is clamped on both sides. Considering the periodic boundary conditions, the system needs to be able to represent a rigid body rotation as mentioned before. Therefore, a simply supported beam is assumed to represent the RVE. Furthermore, the rigid body rotation is removed by adding an additional workless constraint in the center of the system. The described systems are depicted in Fig. 5, with the displacement boundary conditions in the upper part and the periodic boundary conditions in the lower. In both cases, the shear deformation is applied according to Eq. (23). Of course, this deformation leads to a constant shear force Q , and due to Eq. (35) to a linear moment distribution M as depicted in Fig. 5. Assuming further that the system has a bending stiffness of EI and a shear stiffness GA_S , the relationship among the resulting shear force Q , the length of the RVE L_{RVE} and the applied shear deformation γ can be evaluated to

$$\gamma_\alpha = \left(\frac{1}{12EI} L_{RVE}^2 + \frac{1}{GA_S} \right) Q_\alpha \quad \text{with } \alpha = y, z. \tag{36}$$

Without loss of generality, it is assumed that the center of gravity equals the center of shear. Then the relation between the stress resultant Q_α and the shear deformation γ_α must be equal to $Q_\alpha = GA_S \bar{\gamma}_\alpha$. Herein, $\bar{\gamma}_\alpha$ represents an assumed averaged shear deformation. It is obvious that

$$\gamma_\alpha \neq \bar{\gamma}_\alpha = \langle 2E_{x\alpha} \rangle \quad \text{with } \alpha = y, z. \tag{37}$$

Considering Eq. (37), the averaged shear strain $\bar{\gamma}_\alpha$ of the RVE does not equal the applied beam shear strain γ_α due to the equilibrium state. To ensure the equality between $\bar{\gamma}_\alpha$ and γ_α , the linear moment distribution needs to vanish. This can

be established with additional constraints

$$\int_{L_{RVE}} M^y x \, dx = 0 \quad \text{and} \quad \int_{L_{RVE}} M^z x \, dx = 0. \tag{38}$$

Due to the additional constraints according to Eq. (38), the term $L_{RVE}^2/12/EI$ vanishes from Eq. (36). Without this term, the equality $\bar{\gamma}_\alpha = \gamma_\alpha$ between the applied shear deformation and the averaged shear strain is achieved.

4 Finite element implementation

In this section, the numerical treatment of the theory is addressed. To model the macroscopic geometry, displacement-based beam elements are used. On the mesoscopic scale, displacement-based continuum elements are employed. Since they are both standard elements, their numerical realization is not discussed here. The focus is on the treatment of additional constraints and the numerical treatment of the homogenization. While the derivation of the additional constraints follow the approach in [19], but the resulting indefinite matrix will be inverted instead of following the proposed sub-loop approach.

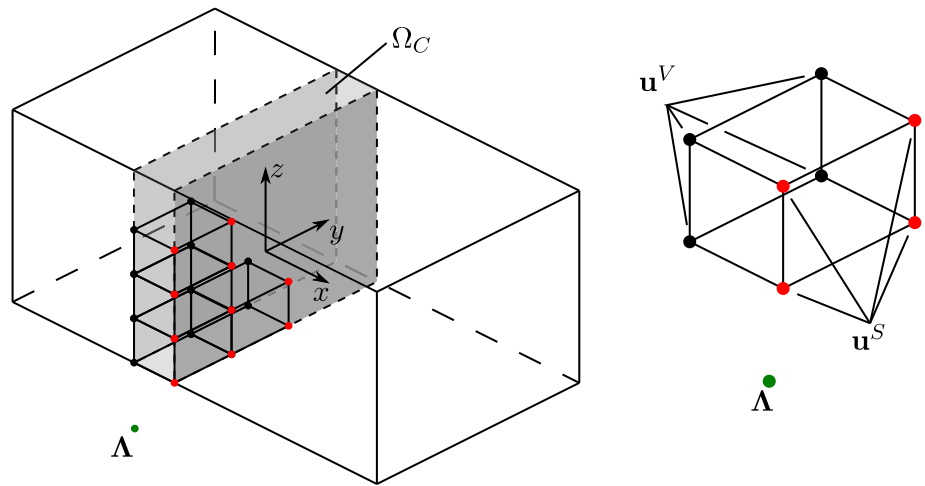
4.1 Constraint of the rigid body rotation

As the beam theory describes the normal stress distribution over a cross-section in a very satisfactory way, a constraint based on this stress component is employed to remove the rigid body rotation. Considering this fact, the constraint can be expressed as

$$\sigma_x - \bar{\sigma}_x = 0, \quad \text{in } \Omega_C. \tag{39}$$

To evaluate the stresses σ_x and $\bar{\sigma}_x$ in Eq. (39), physical and geometrical linearity is assumed. Furthermore, the balance will be enforced in an interface domain Ω_C . Figure 6 shows the assumed geometry of the interface domain Ω_C as well as the finite element mesh and a single finite element. As depicted, the nodes of an element are separated into nel_S nodes on the darker face of the interface domain and nel_V remaining nodes. Additionally, an external node containing

Fig. 6 Rigid body rotation interface—left: geometry with mesh, right: single finite element



the Lagrange parameters is introduced. This node is assigned to each interface element with the special property that it is shared by all of them. The Lagrange parameters are used to enforce the stress assumption according to Eq. (39). As $\bar{\sigma}_x$ will be evaluated using beam kinematics, the constraint must be fulfilled in an average sense and not pointwise. Therefore, only three Lagrange parameters for the entire interface are used, leading to the constraint equation

$$\int_{\Omega_C} (\sigma_x - \bar{\sigma}_x) (\lambda_x + \mu_y z - \mu_z y) \, dV = 0. \tag{40}$$

As the RVE is modeled in the x, y, z -coordinate system with the x -axis as the tangent to the beam axis, the Lagrange parameters can be interpreted as the normal strain λ_x , and the two bending curvatures μ_y and μ_z . With the definitions $\Lambda = [\lambda_x, \mu_y, \mu_z]^T$ and $\bar{\mathbf{p}} = [1, z, -y]^T$, the first variation of Eq. (40) can be derived and added to the weak form of equilibrium

$$g(\mathbf{v}, \delta \mathbf{v}) = \dots + \int_{\Omega_C} \left\{ \bar{\mathbb{C}} (\delta \boldsymbol{\varepsilon}_C - \delta \bar{\boldsymbol{\varepsilon}}_C) \bar{\mathbf{p}} \cdot \Lambda + (\sigma_x - \bar{\sigma}_x) \bar{\mathbf{p}} \cdot \delta \Lambda \right\} \, dV = 0. \tag{41}$$

In Eq. (41), the variations of the stresses ($\delta \sigma_x - \delta \bar{\sigma}_x$) are already replaced by the linear elastic material law $\bar{\mathbb{C}} (\delta \boldsymbol{\varepsilon}_C - \delta \bar{\boldsymbol{\varepsilon}}_C)$. Herein, the vector $\bar{\mathbb{C}} = E / (1 + \nu) / (1 - 2\nu) [1 - \nu, \nu, \nu, 0, 0, 0]$ contains the first line of Hooke’s law in Voigt notation. Thus, the linearization of Eq. (41) reads

$$L[g(\mathbf{v}, \delta \mathbf{v}), \Delta \mathbf{v}] = g(\mathbf{v}, \delta \mathbf{v}) + \dots + \int_{\Omega_C} \left\{ \bar{\mathbb{C}} (\delta \boldsymbol{\varepsilon}_C - \delta \bar{\boldsymbol{\varepsilon}}_C) \bar{\mathbf{p}} \cdot \Delta \Lambda + \bar{\mathbb{C}} (\Delta \boldsymbol{\varepsilon}_C - \Delta \bar{\boldsymbol{\varepsilon}}_C) \bar{\mathbf{p}} \cdot \delta \Lambda \right\} \, dV = 0. \tag{42}$$

With the first variation Eq. (41) and its linearization Eq. (42), only the finite element approximations are missing. For the

geometry and the displacement field, these are done using Lagrange polynomials

$$\mathbf{x}^h = \sum_{I=1}^{nel_V+nel_S} N_I \mathbf{x}_I, \quad \mathbf{u}^h = \sum_{I=1}^{nel_V+nel_S} N_I \mathbf{u}_I, \quad \delta \mathbf{x}^h = \delta \mathbf{u}^h = \sum_{I=1}^{nel_V+nel_S} N_I \delta \mathbf{u}_I, \tag{43}$$

$$\Lambda^h = \Lambda, \quad \delta \Lambda^h = \delta \Lambda.$$

The approximations according to Eq. (43) lead to the first variation of the strains

$$\delta \boldsymbol{\varepsilon}_C^h = \sum_{I=1}^{nel_V+nel_S} \mathbf{B}_I \delta \mathbf{u}_I = \sum_{I=1}^{nel_V+nel_S} \begin{bmatrix} N_{I,x} & 0 & 0 \\ 0 & N_{I,y} & 0 \\ 0 & 0 & N_{I,z} \\ N_{I,y} & N_{I,x} & 0 \\ N_{I,z} & 0 & N_{I,x} \\ 0 & N_{I,z} & N_{I,y} \end{bmatrix} \delta \mathbf{u}_I. \tag{44}$$

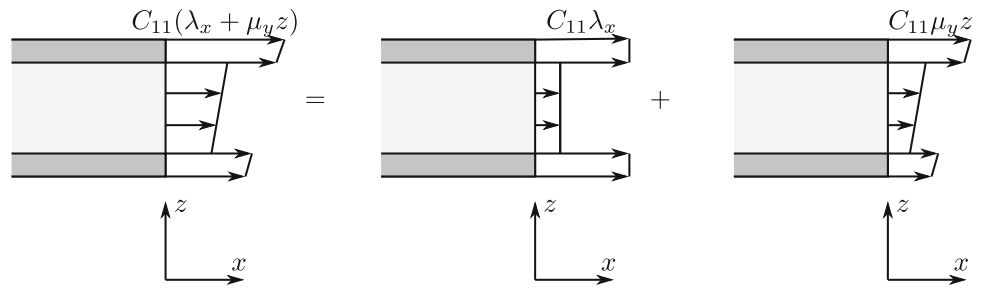
With Eq. (44), the linearization of the strains can be derived by replacing δ with Δ . Regarding the evaluation of the strains $\boldsymbol{\varepsilon}_C^h$ themselves, which are needed to compute $\sigma_x^h = \bar{\mathbb{C}} \boldsymbol{\varepsilon}_C^h$, $\delta \mathbf{u}_I$ is replaced by \mathbf{u}_I in Eq. (44). Next, the assumptions for $\bar{\boldsymbol{\varepsilon}}_C^h$ are chosen as

$$\delta \bar{\boldsymbol{\varepsilon}}_C^h = \sum_{I=1}^{nel_V} \mathbf{B}_I \delta \mathbf{u}_I^V + \sum_{J=1}^{nel_S} \bar{\mathbf{B}}_J \delta \mathbf{u}_J^S$$

$$= \sum_{I=1}^{nel_V} \begin{bmatrix} N_{I,x} & 0 & 0 \\ 0 & N_{I,y} & 0 \\ 0 & 0 & N_{I,z} \\ N_{I,y} & N_{I,x} & 0 \\ N_{I,z} & 0 & N_{I,x} \\ 0 & N_{I,z} & N_{I,y} \end{bmatrix} \delta \mathbf{u}_I^V + \sum_{J=1}^{nel_S} \begin{bmatrix} 0 & 0 & 0 \\ 0 & N_{J,y} & 0 \\ 0 & 0 & N_{J,z} \\ N_{J,y} & N_{J,x} & 0 \\ N_{J,z} & 0 & N_{J,x} \\ 0 & N_{J,z} & N_{J,y} \end{bmatrix} \delta \mathbf{u}_J^S. \tag{45}$$

Regarding Eq. (45), the linearization can again be derived by replacing δ with Δ and the approximation of $\bar{\boldsymbol{\varepsilon}}_C^h$ by dropping δ . Comparing Eq. (45) with Eq. (44), the difference lies in the

Fig. 7 Resulting normal stress at the surface of the interface element constraining a rigid body rotation and a translation in the case of a three-layer structure with two stiff layers and a soft core



computation of the first component of the strain vector $\bar{\epsilon}_C^h$. In this case, the contribution of the displacements u_x^S is set to zero only for this specific strain component of the nodes on the darker surface in Fig. 6. Building the difference between ϵ_C^h and $\bar{\epsilon}_C^h$ yields

$$(\delta \epsilon_C^h - \delta \bar{\epsilon}_C^h) = \sum_{J=1}^{nel_S} \begin{bmatrix} N_{J,x} & 0 & 0 \\ 0 & 0 & 0 \\ 0 & 0 & 0 \\ 0 & 0 & 0 \\ 0 & 0 & 0 \\ 0 & 0 & 0 \end{bmatrix} \delta u_J^S = \tilde{\mathbf{B}} \delta u^S. \quad (46)$$

As Eq. (46) states, only the nodes on the surface nel_S contribute to the constraint equation. And of course, it holds again that $(\Delta \epsilon_C^h - \Delta \bar{\epsilon}_C^h) = \tilde{\mathbf{B}} \Delta u^S$ and $(\epsilon_C^h - \bar{\epsilon}_C^h) = \tilde{\mathbf{B}} u^S$ with $(\sigma_x^h - \bar{\sigma}_x^h) = \bar{\mathbf{C}} (\epsilon_C^h - \bar{\epsilon}_C^h)$. Finally, only the shape functions for the Lagrange parameters are missing, which are assumed to be one. Therefore, the nodal values directly enter the weak form and its linearization. To finalize the element formulation, Eq. (46) needs to be inserted into Eq. (41), which leads to the element load vector

$$[\delta u^V \ \delta u^S \ \delta \Lambda] \mathbf{f}^e = [\delta u^V \ \delta u^S \ \delta \Lambda] \begin{bmatrix} \mathbf{0} \\ \int_{\Omega_C} \tilde{\mathbf{B}}^T \bar{\mathbf{C}}^T \bar{\mathbf{p}} \cdot \Lambda \, dV \\ \int_{\Omega_C} \bar{\mathbf{p}} \bar{\mathbf{C}} \cdot \tilde{\mathbf{B}} u^S \, dV \end{bmatrix}. \quad (47)$$

Furthermore, the stiffness matrix can be derived by inserting Eq. (46) into Eq. (42)

$$\mathbf{k}^e = \begin{bmatrix} \mathbf{0} & \mathbf{0} & \mathbf{0} \\ \mathbf{0} & \mathbf{0} & \mathbf{k}_{ab} \\ \mathbf{0} & \mathbf{k}_{ab}^T & \mathbf{0} \end{bmatrix}, \text{ with } \mathbf{k}_{ab} = \int_{\Omega_C} \tilde{\mathbf{B}}^T \bar{\mathbf{C}}^T \bar{\mathbf{p}}^T \, dV. \quad (48)$$

The integrals in Eqs. (47) and (48) are evaluated employing the Gaussian quadrature rule.

This element was specifically developed to remove the rigid body rotations of the RVE in the case of heterogeneous cross-sections. Therefore, it is formulated in a way that the material parameters are taken into account when distributing the stresses over the cross-section. In view of Eq. (47), the normal stress distribution is exemplarily depicted for a three-layer cross-section in Fig. 7. The jumps in the normal

stress distribution are essential for the correct shear stress distribution through the thickness.

4.2 Linear moment constraint

To remove the linear moment distribution due to the shear deformation, a constraint similar to that used in Sect. 4.1 is proposed. Again, small deformations and linear elastic material behavior are assumed to evaluate the constraints. As the moment, which needs to be removed, results from the normal stresses in x -direction only, the constraint reads

$$\int_{\Omega} \sigma_x (\lambda_x + y\mu_z - z\mu_y) \, dV = 0. \quad (49)$$

This time there is no equivalent beam stress introduced, but the same three Lagrange parameters are used. As before, the Lagrange parameters and the positions can be grouped in $\Lambda = [\lambda_x, \mu_y, \mu_z]^T$ and $\bar{\mathbf{p}} = [1, z, -y]^T$. With this in hand, the weak form of equilibrium gets extended by the first variation of Eq. (49), leading to

$$g(\mathbf{v}, \delta \mathbf{v}) = \dots + \int_{\Omega} (\delta \sigma_x \bar{\mathbf{p}} \cdot \Lambda + \sigma_x \bar{\mathbf{p}} \cdot \delta \Lambda) \, dV = 0. \quad (50)$$

The derivation of the linearization of Eq. (50) is straightforward, leading to

$$L[g(\mathbf{v}, \delta \mathbf{v}), \Delta \mathbf{v}] = g(\mathbf{v}, \delta \mathbf{v}) + \dots + \int_{\Omega} (\delta \sigma_x \bar{\mathbf{p}} \cdot \Delta \Lambda + \Delta \sigma_x \bar{\mathbf{p}} \cdot \delta \Lambda) \, dV = 0. \quad (51)$$

The linearization of the weak form Eq. (51) looks quite comparable to Eq. (42), with the main difference being that the integration is performed over the whole RVE. This means that, in contrast to the rigid body rotation constraint, the Lagrange parameters are global to the whole RVE and not only to certain elements. Additionally, they are constant in the y, z -plane, but get assigned appropriate shape functions in the x -direction in order to remove the linear moment distribution based on the chosen boundary conditions according to Sect. 3.2. Therefore, by means of the finite element approximation, the shape functions for the Lagrange parameters in

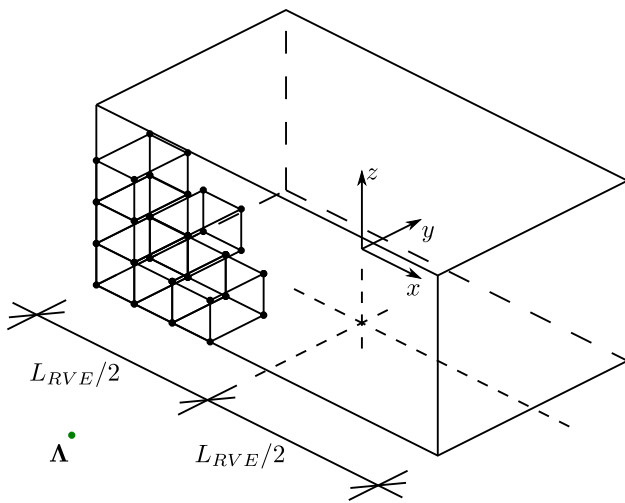


Fig. 8 Finite element mesh for the linear moment constraint

the x -direction are

$$N_{\Lambda} = \begin{cases} x & \text{displacement b. c.} \\ \begin{cases} x + \frac{1}{2}L_{RVE}, & x < 0 \\ x - \frac{1}{2}L_{RVE}, & x > 0 \end{cases} & \text{periodic b. c.} \end{cases} \quad (52)$$

The displacement field is approximated by standard Lagrange polynomials. Therefore, the final approximations read

$$\begin{aligned} \mathbf{x}^h &= \sum_{I=1}^{nel} N_I \mathbf{x}_I, & \mathbf{u}^h &= \sum_{I=1}^{nel} N_I \mathbf{u}_I, & \delta \mathbf{x}^h &= \delta \mathbf{u}^h = \sum_{I=1}^{nel} N_I \delta \mathbf{u}_I, \\ \Lambda^h &= N_{\Lambda} \Lambda, & \delta \Lambda^h &= N_{\Lambda} \delta \Lambda. \end{aligned} \quad (53)$$

Again, the linearizations are derived by replacing δ with Δ . With the finite element approximations according to Eq. (53), the constraint requires the entire RVE mesh as well as an additional node with Lagrange parameters Λ .

This can be achieved by using the already generated mesh of the RVE to interpolate the displacement field and add a shared node to all elements, as depicted in Fig. 8. To derive the element load vector, Eq. (53) just needs to be inserted into Eq. (50)

$$[\delta \mathbf{u}^h \ \delta \Lambda^h] \mathbf{f}^e = [\delta \mathbf{u}^h \ \delta \Lambda^h] \begin{bmatrix} \int_V \mathbf{B}^T \bar{\mathbf{C}}^T \bar{\mathbf{p}} \cdot \Lambda^h \, dV \\ \int_V N_{\Lambda} \bar{\mathbf{p}} \bar{\mathbf{C}} \cdot \mathbf{B}^T \mathbf{u} \, dV \end{bmatrix}. \quad (54)$$

Finally, the element stiffness matrix can be derived by the linearization of Eq. (54)

$$\mathbf{k}^e = \begin{bmatrix} \mathbf{0} & \mathbf{k}_{ab} \\ \mathbf{k}_{ab}^T & \mathbf{0} \end{bmatrix}, \quad \text{with } \mathbf{k}_{ab} = \int_V \mathbf{B}^T \bar{\mathbf{C}}^T \bar{\mathbf{p}}^T N_{\Lambda} \, dV. \quad (55)$$

With Eqs. (54) and (55), the element is completely described. However, special considerations regarding the element load vector are necessary. Reconsidering $\bar{\mathbf{C}} = E / (1 + \nu) / (1 - 2\nu) [1 - \nu, \nu, \nu, 0, 0, 0]$ with the components in Voigt notation $[\mathbb{C}_{11}, \mathbb{C}_{12}, \mathbb{C}_{13}, \mathbb{C}_{14}, \mathbb{C}_{15}, \mathbb{C}_{16}]$ and evaluating Eq. (54) leads to

$$\mathbf{f}_{1I}^e = \int_V \begin{bmatrix} N_{I,x} \mathbb{C}_{11} \\ N_{I,y} \mathbb{C}_{12} \\ N_{I,z} \mathbb{C}_{13} \end{bmatrix} \bar{\mathbf{p}} \cdot \Lambda^h \, dV. \quad (56)$$

Keeping the load vector as in Eq. (56) would just shift the problem from the stresses in length direction to the stresses in thickness direction of the beam. At this point, there are two possibilities. Either repeating the constraint for σ_y and σ_z or setting the Poisson’s ratio to zero. The first choice leads to additional unknown Lagrange parameters. Therefore, the Poisson’s ratio will be assumed to be zero for the numerical examples.

4.3 Homogenization algorithm

The basis of the homogenization algorithm is in accordance with [9]. To derive a consistently linearized formulation leading to a quadratic convergence of the coupled model, the weak form of equilibrium of the macroscopic model is extended with homogenized mesoscopic models. Assuming Voigt notation, the equation of the coupled model reads

$$\begin{aligned} g(\mathbf{v}, \delta \mathbf{v}) &= \int_{\Omega^M} \delta \mathbf{E}^M \cdot \mathbf{S}^M \, dV + \{\text{load terms}\}^M \\ &+ \sum_{i=1}^{numel \cdot ngp} \frac{1}{L_{RVE,i}} \int_{\Omega_i} \delta \mathbf{E} \cdot \mathbf{S} \, dV = 0. \end{aligned} \quad (57)$$

The weak form of equilibrium in Eq. (57) contains the macroscopic model denoted with $\{\bullet\}^M$ as well as mesoscopic models for which a special identification is omitted. As stated in Eq. (57), each of the $numel$ macroscopic elements gets assigned one individual RVE for each of its ngp integration points. The integration of RVEs is performed over their volume Ω_i , while the homogenization is performed over the length of the RVE $L_{RVE,i}$, which is calculated based on the extent of the RVE in the x -direction.

To achieve quadratic convergence using the Newton-Raphson scheme, a consistent linearization of the weak form of equilibrium Eq. (57) is necessary. This leads to the following expression:

$$L[g(\mathbf{v}, \delta \mathbf{v}), \Delta \mathbf{v}] := g(\mathbf{v}, \delta \mathbf{v}) + Dg \cdot \Delta \mathbf{v} = 0. \quad (58)$$

Inserting the finite element shape functions into Eq. (58) yields the following system of equations:

$$L [g(\mathbf{v}, \delta \mathbf{v}), \Delta \mathbf{v}] = \sum_{e=1}^{numel} \begin{bmatrix} \delta \mathbf{v}^M \\ \delta \mathbf{V}_1 \\ \vdots \\ \delta \mathbf{V}_{ngp} \end{bmatrix}_e^T \left\{ \begin{bmatrix} \mathbf{k}^M & \mathbf{0} & \dots & \mathbf{0} \\ \mathbf{0} & \mathbf{K}_1 & \dots & \mathbf{0} \\ \vdots & \vdots & \ddots & \vdots \\ \mathbf{0} & \mathbf{0} & \dots & \mathbf{K}_{ngp} \end{bmatrix} \begin{bmatrix} \Delta \mathbf{v}^M \\ \Delta \mathbf{V}_1 \\ \vdots \\ \Delta \mathbf{V}_{ngp} \end{bmatrix} + \begin{bmatrix} \mathbf{f}^M \\ \mathbf{F}_1 \\ \vdots \\ \mathbf{F}_{ngp} \end{bmatrix} \right\} = 0. \tag{59}$$

To get better insight, Eq. (59) expresses the system of equations as a summation of all macroscopic elements e . As already stated, each macroscopic element gets assigned one RVE for each of its integration points. Due to the structure of the resulting equation system, each RVE can be solved independently. Therefore, to perform the numerical homogenization it is enough to look at one single RVE. Here, RVE i out of the $1 \dots ngp$ RVEs is considered. It is assumed that the numerical model consists of $numel2$ finite elements, which are identified by \bar{e} . The equation system of one RVE can then be expressed as a sum of all elements \bar{e} , and the relation between elementwise displacements and system displacements as well as macroscopic strains can be expressed as

$$\mathbf{v}_{\bar{e}} = \begin{bmatrix} \mathbf{v}_a \\ \mathbf{v}_b \end{bmatrix}_{\bar{e}} = \begin{bmatrix} \mathbf{a}_{\bar{e}} & \mathbf{0} \\ \mathbf{0} & \mathbf{A}_{\bar{e}} \end{bmatrix} \begin{bmatrix} \mathbf{V} \\ \boldsymbol{\varepsilon} \end{bmatrix}. \tag{60}$$

In this contribution, the values $\boldsymbol{\varepsilon}$ in Eq. (60) contain the beam strains from Sect. 2. The matrix $\mathbf{a}_{\bar{e}}$ is the standard assembly matrix, while the matrix $\mathbf{A}_{\bar{e}}$ can be evaluated using the matrix \mathbf{A} of Eq. (5) by replacing ξ_2 with y and ξ_3 with z . This leads to $\mathbf{A}_{\bar{e}} = \hat{x}\mathbf{A}$, where \hat{x} is the x -coordinate of the node that corresponds to \mathbf{v}_b .

Furthermore, the same relations are assumed for the virtual as well as the linearized values, leading to

$$\begin{aligned} \delta \mathbf{v}_{\bar{e}} &= \begin{bmatrix} \delta \mathbf{v}_a \\ \delta \mathbf{v}_b \end{bmatrix} = \begin{bmatrix} \mathbf{a}_{\bar{e}} & \mathbf{0} \\ \mathbf{0} & \mathbf{A}_{\bar{e}} \end{bmatrix} \begin{bmatrix} \delta \mathbf{V} \\ \delta \boldsymbol{\varepsilon} \end{bmatrix}, \\ \Delta \mathbf{v}_{\bar{e}} &= \begin{bmatrix} \Delta \mathbf{v}_a \\ \Delta \mathbf{v}_b \end{bmatrix} = \begin{bmatrix} \mathbf{a}_{\bar{e}} & \mathbf{0} \\ \mathbf{0} & \mathbf{A}_{\bar{e}} \end{bmatrix} \begin{bmatrix} \Delta \mathbf{V} \\ \Delta \boldsymbol{\varepsilon} \end{bmatrix}. \end{aligned} \tag{61}$$

Expressing the equation system of one RVE as the sum over all its elements and inserting Eq. (61) leads to

$$\delta \mathbf{V}^T (\mathbf{K} \Delta \mathbf{V} + \mathbf{F}) = \frac{1}{L_{RVE}} \sum_{\bar{e}=1}^{numel2} \begin{bmatrix} \delta \mathbf{V} \\ \delta \boldsymbol{\varepsilon} \end{bmatrix}^T \left\{ \begin{bmatrix} \mathbf{a}_{\bar{e}}^T \mathbf{k}_{aa} \mathbf{a}_{\bar{e}} & \mathbf{a}_{\bar{e}}^T \mathbf{k}_{ab} \mathbf{A}_{\bar{e}} \\ \mathbf{A}_{\bar{e}}^T \mathbf{k}_{ba} \mathbf{a}_{\bar{e}} & \mathbf{A}_{\bar{e}}^T \mathbf{k}_{bb} \mathbf{A}_{\bar{e}} \end{bmatrix} \begin{bmatrix} \Delta \mathbf{V} \\ \Delta \boldsymbol{\varepsilon} \end{bmatrix} + \begin{bmatrix} \mathbf{a}_{\bar{e}}^T \mathbf{f}_a \\ \mathbf{A}_{\bar{e}}^T \mathbf{f}_b \end{bmatrix} \right\}. \tag{62}$$

Furthermore, the following matrices are introduced:

$$\begin{aligned} \mathbf{K} &= \sum_{e=1}^{numel2} \mathbf{a}_e^T \mathbf{k}_{aa} \mathbf{a}_e & \mathbf{F}_a &= \sum_{e=1}^{numel2} \mathbf{a}_e^T \mathbf{f}_a \\ \mathbf{L} &= \sum_{e=1}^{numel2} \mathbf{a}_e^T \mathbf{k}_{ab} \mathbf{A}_e & \mathbf{F}_b &= \sum_{e=1}^{numel2} \mathbf{A}_e^T \mathbf{f}_b \\ \mathbf{M} &= \sum_{e=1}^{numel2} \mathbf{A}_e^T \mathbf{k}_{bb} \mathbf{A}_e. \end{aligned} \tag{63}$$

In a next step, a static condensation of the internal degrees of freedom $\Delta \mathbf{V}$ and a comparison to the virtual internal work of the macroscopic scale can be performed. This leads to the expression

$$\begin{aligned} &\frac{1}{L_{RVE}} \left\{ \delta \boldsymbol{\varepsilon} \cdot (\mathbf{F}_b - \mathbf{L}^T \mathbf{K}^{-1} \mathbf{F}_a) + \delta \boldsymbol{\varepsilon} \cdot (\mathbf{M} - \mathbf{L}^T \mathbf{K}^{-1} \mathbf{L}) \Delta \boldsymbol{\varepsilon} \right\} \\ &= \{ \delta \boldsymbol{\varepsilon} \cdot \boldsymbol{\sigma} + \delta \boldsymbol{\varepsilon} \cdot \mathbf{D} \Delta \boldsymbol{\varepsilon} \}. \end{aligned} \tag{64}$$

A comparison of the variables in Eq. (64) leads to the definition of the stress resultants and material tangent. They are given as

$$\boldsymbol{\sigma} = \mathbf{F}_b - \mathbf{L}^T \mathbf{K}^{-1} \mathbf{F}_a \quad \text{and} \quad \mathbf{D} = \mathbf{M} - \mathbf{L}^T \mathbf{K}^{-1} \mathbf{L}. \tag{65}$$

The values in Eq. (65) of the numerical homogenization scheme enter the macroscopic beam element. Thus, the entire schema is defined consistently linearized.

5 Numerical examples

In this section selected numerical examples are presented with a focus on the improvement of the results due to the introduced additional constraints. Summing up Sect. 3 and 4, three different kinds of boundary conditions are used. They are displacement boundary conditions (DBC), displacement boundary conditions with linear moment constraints Eq. (49) (DBCC) and the periodic boundary conditions with rigid body rotation constraints Eq. (40) and linear moment constraints Eq. (49) (PBCC). They can be abstractly visualized as depicted in Fig. 9. In the case of DBC, according to Fig. 9a, the displacement component in the length direction u_x on sides x^+ and x^- is fixed. Remaining displacements on these sides are assumed periodic to reduce boundary effects. For DBCC the same assumptions are made as for DBC, but linear moment constraints from Sect. 4.2 are applied, as displayed in Fig. 9b. The third set, the PBCC, is shown in Fig. 9c. Here, the whole displacement field on the sides x^+ and x^- is assumed periodic. Additionally, the rigid body rotations are removed by applying the interface element according to Sect. 4.1 in the center of the RVE. Finally, linear moment

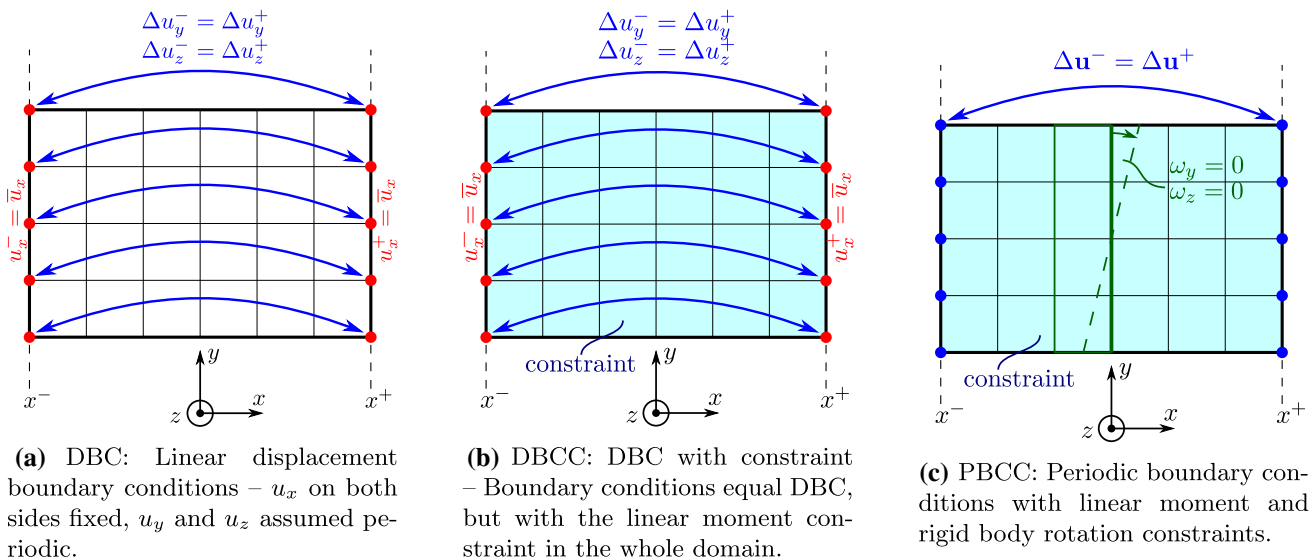
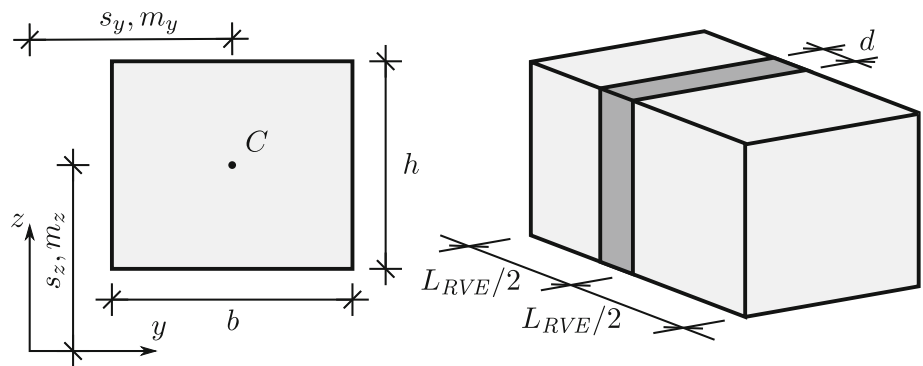


Fig. 9 RVE – Side view of mesh with boundary conditions

Fig. 10 Cross-section geometry on the left and RVE geometry on the right



distributions are removed by the linear moment constraints according to Sect. 4.2.

To avoid repetition of the description of the used finite elements, a displacement-based beam formulation with linear Lagrange shape functions and one-point integration is used. For the volume elements, a displacement-based formulation with tri-quadratic Lagrange shape functions is employed. When other formulations are used, it is explicitly stated.

5.1 Rectangular cross-section

The first example is a rectangular cross-section. This simple example is used as a benchmark test, as its linear cross-sectional properties are well known. Its geometry as well as a schematic plot of the corresponding RVE is visualized in Fig. 10. The cross-section has a width of b and a height of h , and the RVE has a length of L_{RVE} . Furthermore, the coordinates of the center of gravity are denoted as s_y and s_z . The same applies for the position of the center of shear, the coordinates of which are denoted m_y and m_z . As the interface

according to Sect. 4.1 is a 3D element, its thickness is called d with a value of $d = L_{RVE}/10$.

5.1.1 Linear elasticity: centered cross-section

At first, effective cross-sectional values are evaluated considering the beam axis goes through the center of gravity of the cross-section ($s_y = m_y = s_z = m_z = 0$ cm). The size of the cross-section is chosen as $b = h = 1$ cm. Regarding the material parameters, a Young’s modulus of $E = 21,000$ kN cm⁻² and a Poisson’s ratio of $\nu = 0.3$ are used.

To show the improvement due to the introduced additional constraints, the length L_{RVE} is varied. Furthermore, cross-sectional values are evaluated analytically and are given in Table 1. For the shear stiffness, a shear correction factor of $\kappa = 5/6$ is considered.

The finite element mesh consists of 4×4 elements over the cross-section with 8 elements along the length of the RVE in the case of DBC and 9 elements along the length in the case of PBCC due to rotational constraints.

Table 1 Effective cross-sectional values of the rectangular cross-section

EA	GA_S	EI	GI_T
21,000 kN	6730 kN	1750 kN cm ²	1130 kN cm ²

Results for tension stiffness EA and bending stiffness EI are given in Fig. 11. For both stiffnesses, the results of the numerical homogenization scheme are independent of the length of the RVE and match the analytical solution, see Fig. 11.

The results for shear and torsional stiffnesses are depicted in Fig. 12. If DBC or DBCC are used, they depend on the length of the RVE, as cross-sectional warping needs to be considered. While the torsional stiffness GI_T converges to the analytical value with increasing length, the shear stiffness GA_S converges to zero in the case of DBC. Using DBCC, homogenized shear stiffness converges to the analytical solution. In the case of the proposed PBCC, results of the homogenization scheme are independent of the length L_{RVE} of the RVE and match the analytical solution.

The influence of linear moment constraints is depicted in Fig. 13a. Herein, the RVE stays straight under a shear deformation employing PBCC, and cross-sectional warping occurs. It is worth mentioning that the stress boundary conditions on top and on bottom of the RVE are fulfilled. In the case of DBC, the cross-sectional warping is suppressed, and an additional deformation due to the linear moment distribution is clearly visible in Fig. 13b. This deformation is responsible for the length dependency of the shear stiffnesses when performing the numerical homogenization.

To close this example, mesh convergence of resulting shear and torsional stiffnesses is investigated and depicted in Fig. 14. In this case, only the cross-section is refined, while the number of elements along the length is kept constant. The underlying reference solution for the shear stiffness

assumes a shear correction factor of $\kappa = 5/6$, and the reference solution for the torsional stiffness is evaluated to $GI_T = 1135.4297$ kN cm² using the element given in [12]. It is worth mentioning that results for tension and bending stiffnesses are numerically exact for the initial mesh.

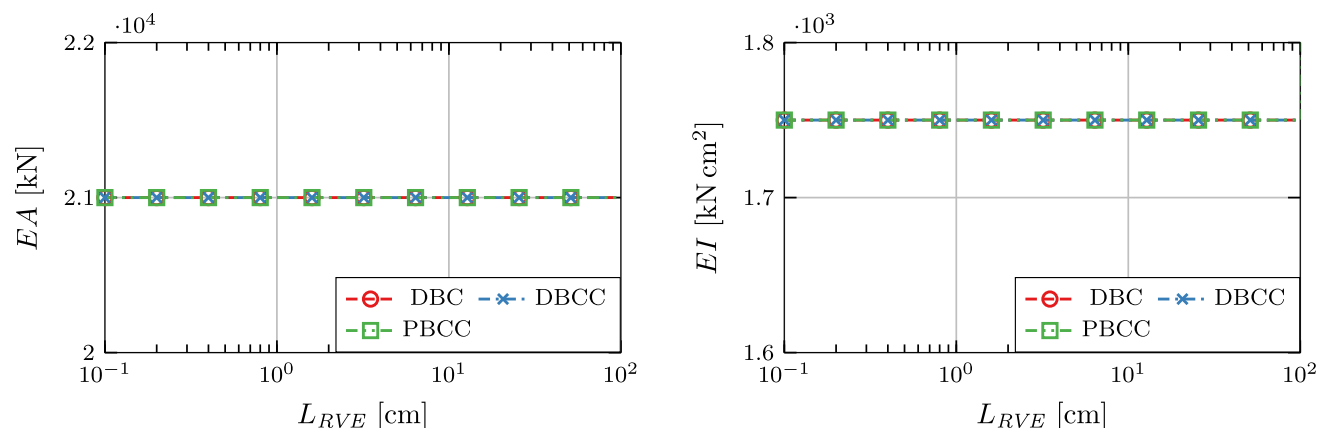
5.1.2 Off-centered cross-section

In this example the same rectangular cross-section is assumed, but an off-centered cross-section is investigated. As a reference solution, cross-sectional values are evaluated according to Eq. (18). The eccentricity is chosen as $s_y = m_y = 1$ cm and $s_z = m_z = 0$ cm. Remaining parameters are the same as in the previous example.

As all boundary conditions yield numerically exact tension and bending stiffnesses, the focus is on torsional stiffness, which depends on the distance from the center of shear to the beam axis as well as the effective shear area. Again, the influence of the length of the RVE is investigated. The reference value for torsional stiffness is assumed as $GI_T^* = 1135.4297$ kN cm² and accounting for eccentricity as $G(I_T^* + m_y^2 A_S) = 7871.908$ kN cm². As depicted in Fig. 15, solutions are again independent of the length of the RVE and equal the reference solution of Eq. (18) employing PBCC. In contrast to this, the DBC case shows a length dependency and decreases against the solution of the centered cross-section. This is because the effective shear stiffness drops to zero as length increases.

5.1.3 Cantilever beam: considering plasticity

To leave the linear elastic regime and to show that the scheme can consider physical nonlinearities, a bending-dominated problem including plasticity is investigated. The example is taken from [17,26]. This time the rectangular cross-section has a width of $b = 2$ and a height of $h = 1$. The beam axis goes through the center of gravity of the cross-section;

**Fig. 11** Results of the homogenization scheme for EA and EI in the case of varying RVE length—rectangular cross-section

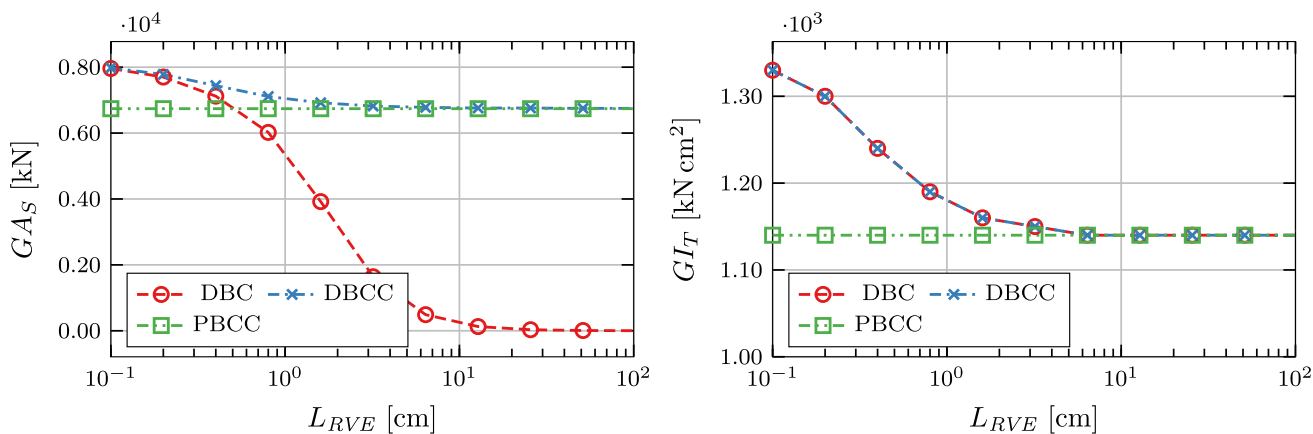


Fig. 12 Results of the homogenization scheme for GA_S and GI_T in the case of varying RVE length – Rectangular cross-section

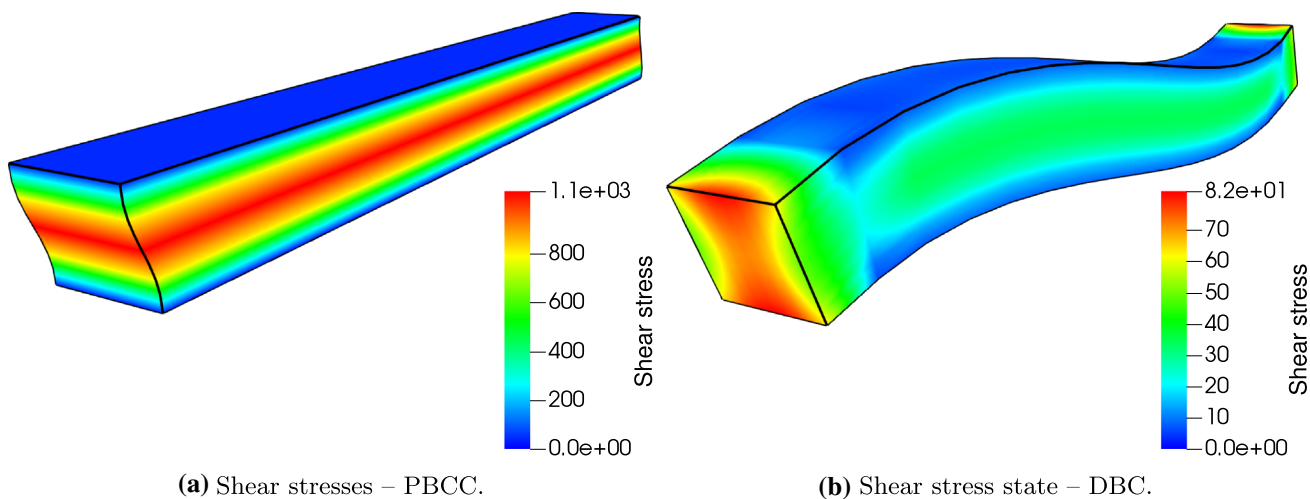


Fig. 13 Shear deformation and shear stresses in ($kN\ cm^{-2}$) of RVEs with different boundary conditions—rectangular cross-section

Fig. 14 Mesh convergence of PBCC—regular refinement of the cross-section with a constant number of elements in length direction

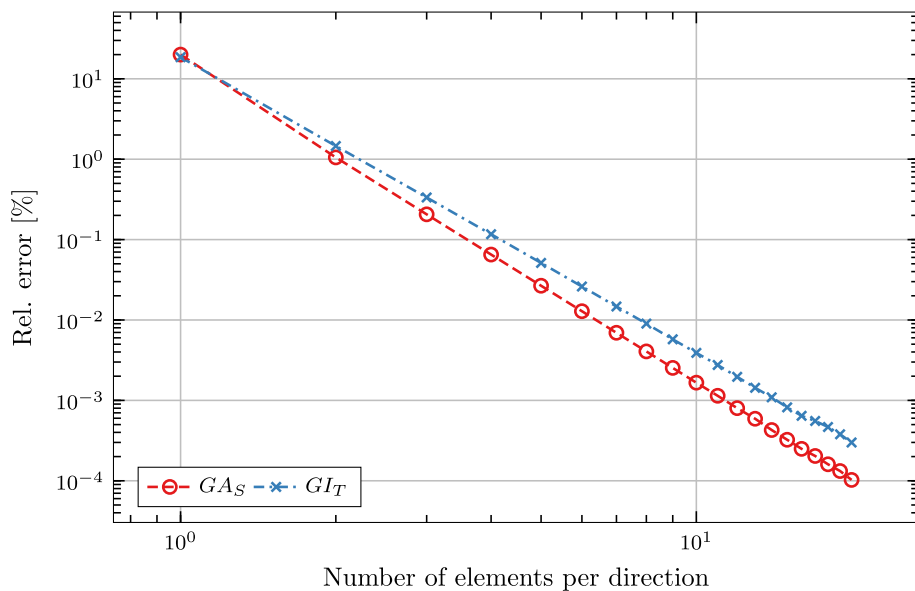


Fig. 15 Resulting torsional stiffness in the case of an eccentricity of $s_y = m_y = 1$ cm

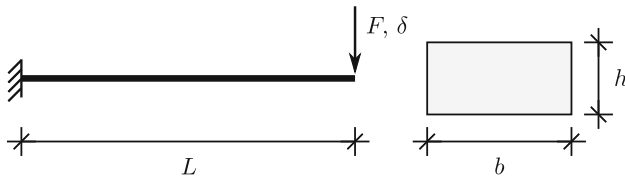
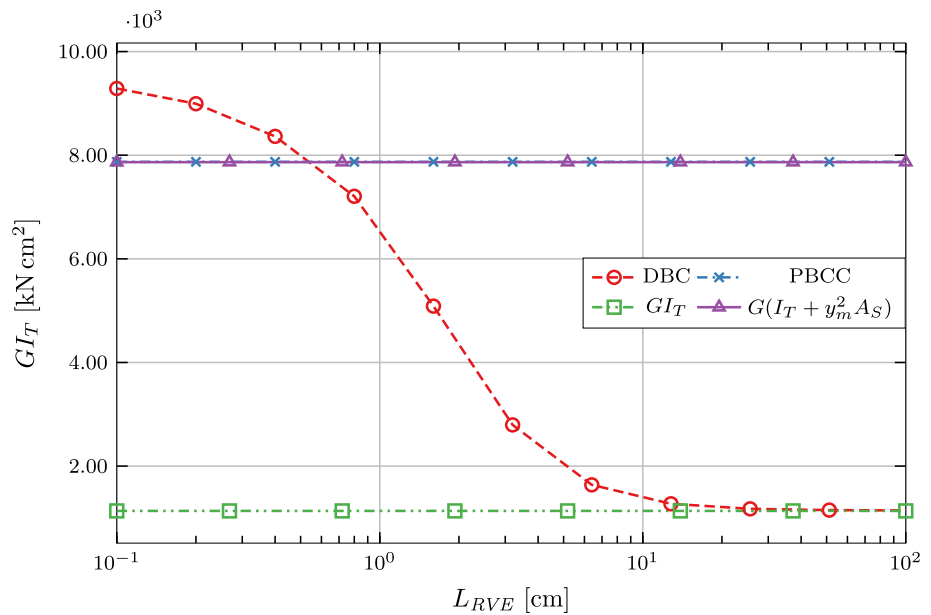


Fig. 16 Geometry of the cross-section and the cantilever beam with load

this means $s_y = m_y = s_z = m_z = 0$. The length of the cantilever is $L = 20$. As already stated, a plastic material behavior is assumed with a Young’s modulus of $E = 16000$, a Poisson’s ratio of $\nu = 0.3$, a yield stress of $Y_0 = 20$ and a hardening modulus of $H = 200$. Additionally, on both scales geometrical nonlinearity is assumed.

The geometry of the system with load is depicted in Fig. 16. For the macroscopic system, 20 linear beam elements are chosen, and the RVE is meshed with 8 elements over its width, 4 elements over its height, and 8 elements along its length in the case of DBC, 3 elements along its length for PBCC. The length of the RVE is chosen as $L_{RVE} = 1$ for both boundary conditions. For the PBCC, again a thickness of $d = L_{RVE}/10$ for the rotational interface is chosen.

Figure 17 shows the results of the scheme with DBC and PBCC and compares them to the reference solution (Ref.) from [17,26] and a full 3D model. Here, force F is plotted versus the deflection δ . Calculations with DBC and PBCC agree well with the reference solutions.

To show that results of the proposed coupled model depend on the length of the RVE L_{RVE} in the case of DBC and are independent of its length in the case of PBCC, the macroscopic model is slightly modified. The length of the beam will be reduced to $L = 6$. Therefore, the length to

height ratio shrinks to $L/h = 6$, and the impact of shear deformation on the total deflection increases.

Results of the calculation are depicted in Fig. 18. Here, to further distinguish among them, the names of the RVE boundary conditions are extended with the length of the RVE; for example, DBC1 means that displacement boundary conditions with an RVE length $L_{RVE} = 1$ are used. It is noticeable that results using PBCC are the same whether the length of the RVE is chosen as $L_{RVE} = 1$ (PBCC1) or $L_{RVE} = 6$ (PBCC6). In the case of the DBC, the coupled model leads to comparable results if the RVE has a length of $L_{RVE} = 1$ (DBC1). If its length is increased to $L_{RVE} = 6$ (DBC6), even the linear part of the load deflection curve is too soft, and the maximum load is underestimated.

5.1.4 Torsional limit load considering plasticity

To further investigate the influence of RVE length, the limit load due to torsional moment is investigated. The example is taken from [28]. Here, the cross-section has a height of $h = 10$ cm and a width of $b = 5$ cm. The beam axis goes through the center of gravity of the cross-section, which equals the center of shear in this case ($s_y = s_z = m_y = m_z = 0$ cm). Furthermore, an isotropic linear elastic, ideal plastic material law with a Young’s modulus of $E = 21,000$ kN cm⁻², a Poisson’s ratio of $\nu = 0.3$ and a yield stress of $Y_0 = 24$ kN cm⁻² is chosen. Here, only shear stresses are responsible for the occurrence of plasticity. They are limited to a value of $\tau_{max} = 13.86$ kN cm⁻². According to [28], the limit state can be computed as

$$M_T^el = 0.246 \cdot \tau_{max} \cdot h \cdot b^2 = 852.2 \text{ kN cm}$$

Fig. 17 Load deflection curve—load F versus deflection δ

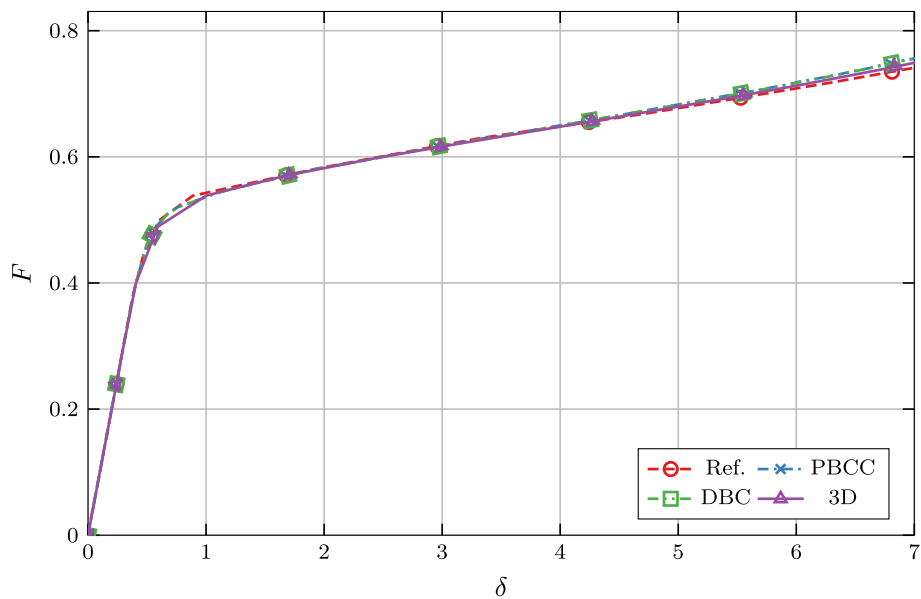
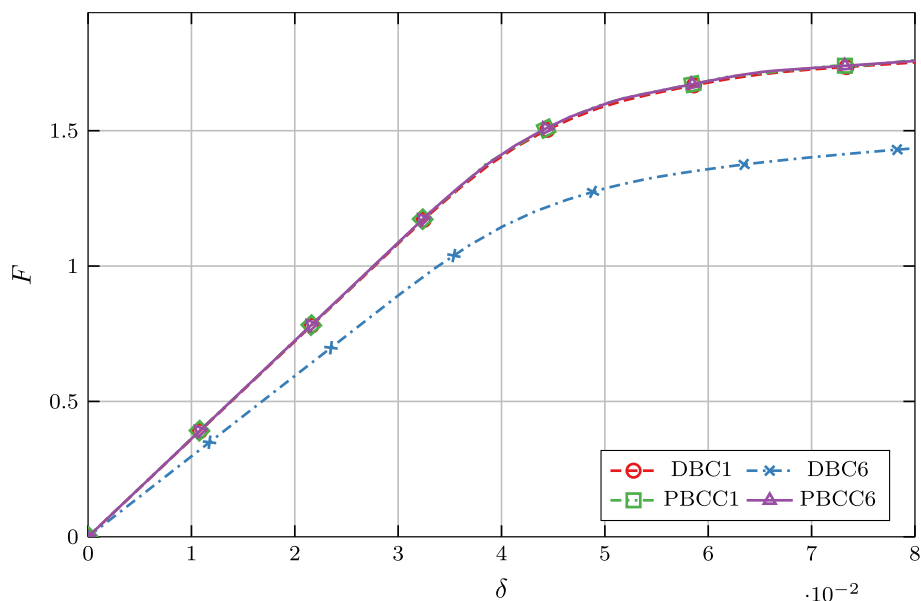


Fig. 18 Load deflection curve with varying RVE length—load F versus deflection δ



$$\text{and } M_T^{pl} = \frac{1}{6} \cdot \tau_{max} \cdot b^2 \cdot (3 \cdot h - b) = 1443.4 \text{ kN cm.} \tag{66}$$

Values in Eq. (66) are the elastic limit torsional moment M_T^{el} and the plastic one M_T^{pl} .

With previously given values, two directions of the RVEs are defined. The remaining direction is chosen as $L_{RVE} = 5$ cm in the case of PBCC, again with an interface thickness of $d = L_{RVE}/10$. For DBC, the length will be varied and is attached to its name, as in the last example. Therefore, the RVE in the case of DBC20 has the length $L_{RVE} = 20$ cm and in the case of DBC100 the length is $L_{RVE} = 100$ cm. The mesh of the RVEs is chosen with 8 elements in height and 4 elements in width. The length direction is meshed with 3

elements in the case of PBCC and 8 elements in the case of DBC. The finer mesh in the case of DBC is chosen because of the suppressed warping.

Results of the calculation are depicted in Fig. 19. On the left side, PBCC and DBC are compared to the analytical solution according to Eq. (66). As expected, the DBC20 with an RVE length of $L_{RVE} = 20$ cm show a too stiff behavior due to the warping constraint. This affects not only the linear elastic part but leads to an overestimation of the maximum torsional moment as well. If the length of the RVE is increased to $L_{RVE} = 100$ cm, results look much better, as seen for DBC100. In comparison with Fig. 12, however, the shear stiffness is underestimated, whereas when using the PBCC, results are independent of the length of the RVE

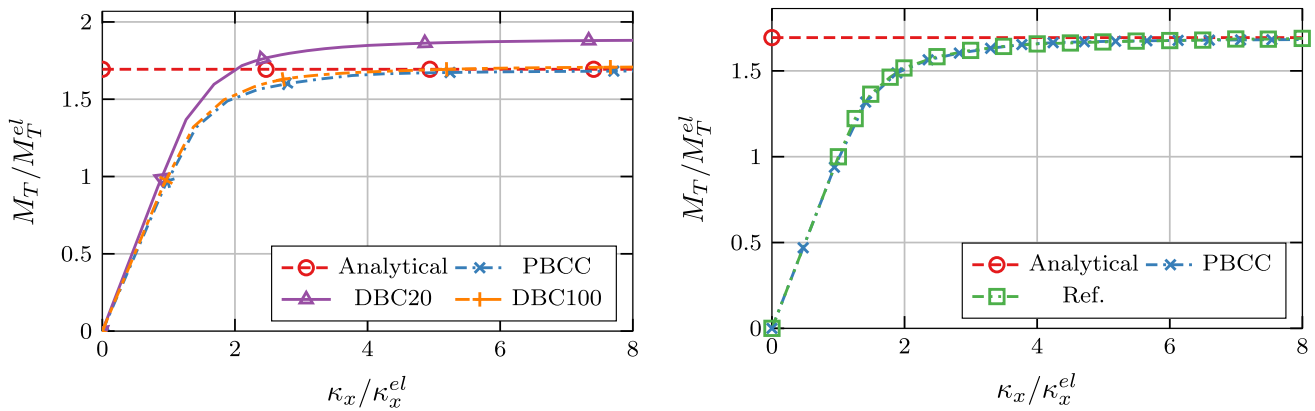


Fig. 19 Load deflection behavior—normalized moment versus normalized torque

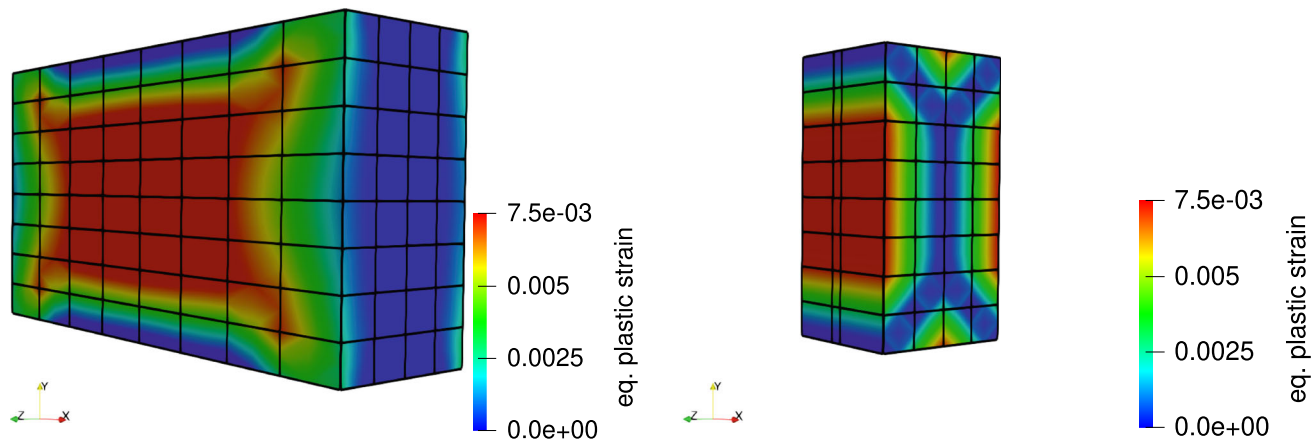


Fig. 20 Comparison of the equivalent plastic strain in the full plastic state—DBC20 on the left and PBCC on the right

L_{RVE} . Furthermore, the reference solution (Ref.) of [28] is in good agreement with the solution of PBCC, see Fig. 19 on the right.

To get insight into what is happening on the mesoscopic scale, the equivalent plastic strain in the case of a fully plastic state for DBC20 and PBCC are depicted in Fig. 20. On the left side, the strain state of DBC20 is depicted. The boundary effects on the strain state are clearly noticeable. In contrast to that, the constraints due to PBCC have no impact on the strain state as shown in the picture on the right.

5.2 U-shaped profile

To show the necessity of an accurate approximation of shear stiffnesses within the multiscale scheme, a U-shaped profile is investigated. The crucial property is that the center of shear does not equal the center of gravity for this cross-section.

Figure 21 shows the geometry of the cross-section. The geometrical data are height $h = 10$ cm, width $b = 10$ cm, thickness of the web $s = 0.6$ cm and thickness of the flanges $t = 1.2$ cm. Furthermore, the parameters $n_c = n_w = 4$ specify the numbers of elements used to mesh the cross-section.

Along the RVE's length, 10 elements are used. As a result, the thickness of the rotational interface is $d = L_{RVE}/10$. A homogeneous, isotropic material behavior with a Young's modulus of $E = 21,000$ kN cm $^{-2}$ and a Poisson's ratio of $\nu = 0.3$ is assumed.

5.2.1 Effective properties

As a reference solution, the cross-sectional properties given in Table 2 are calculated with the elements in [8,12]. The distances to the center of gravity s_y and s_z as well as the distances to the center of shear m_y and m_z are provided with respect to the lower left corner of the cross-section according to Fig. 21. Furthermore, the listed shear correction factors κ_y and κ_z lead to the resulting shear stiffnesses $GA_{S_y} = \kappa_y GA$ and $GA_{S_z} = \kappa_z GA$. The torsion constant I_T^* is given with respect to the center of shear and can be calculated with respect to the center of gravity as $I_T = 310.018$ cm 4 according to Eq. (18).

Using the homogenization scheme with PBCC leads to the cross-sectional values given in Table 3. Here, RVE lengths L_{RVE} of 1 cm and 100 cm are chosen. Both cases give the

Fig. 21 Geometric description of the cross-section

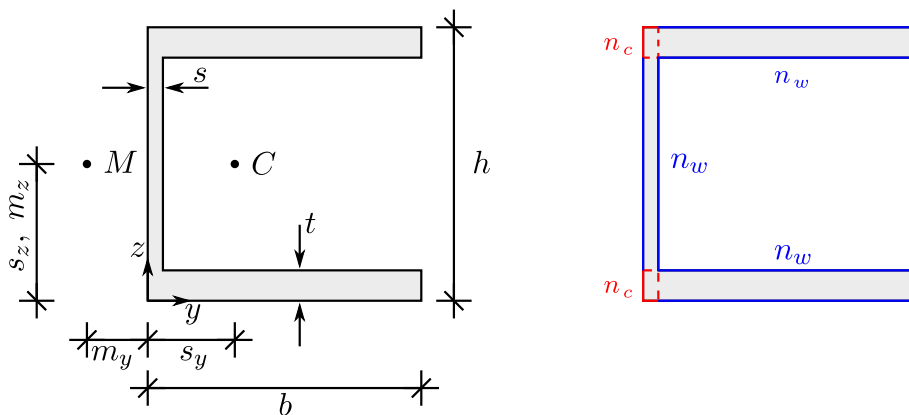


Table 2 Cross-sectional properties of the U-shaped profile

A	I_y		I_z		I_T^*
28.56 cm ²	489.4688 cm ⁴		284.78419 cm ⁴		11.293598 cm ⁴
s_y	s_z	m_y	m_z	χ_y	χ_z
4.2495798 cm	5 cm	4.0828184 cm	5 cm	0.659 10048	0.150 65091

Table 3 Cross-sectional values of the homogenization scheme using PBCC for $L_{RVE} = 1$ cm and $L_{RVE} = 100$ cm

$L_{RVE} = 1$ cm					
A	I_y		I_z		I_T^*
28.56 cm ²	489.469 cm ⁴		284.784195 cm ⁴		11.39699501 cm ⁴
s_y	s_z	m_y	m_z	χ_y	χ_z
4.24958 cm	5 cm	4.0770323 cm	4.9999989 cm	0.66221	0.151 97
$L_{RVE} = 100$ cm					
A	I_y		I_z		I_T^*
28.56 cm ²	489.469 cm ⁴		284.784195 cm ⁴		11.39699501 cm ⁴
s_y	s_z	m_y	m_z	χ_y	χ_z
4.24958 cm	5 cm	4.0770323 cm	4.9999989 cm	0.66221	0.15197

same results and are consistent with the reference solution in Table 2.

Using DBC, the tension and bending stiffnesses are calculated numerically exactly, but length-dependent results for the cross-sectional values are observed if they arise from shear stresses, see Fig. 22. Within this diagram, results are normalized by the reference solutions given in Table 2. The length dependency of the position of the center of shear resides in the suppressed warping. Therefore, it is not connected to the problem described in Sect. 3.2, but is a general problem of DBC due to the suppressed warping and is resolved by increasing the length L_{RVE} of the RVE. In contrast, the shear stiffnesses drop to zero again, and connected to them, the torsional stiffness converges to the value related to the center of shear.

5.2.2 Lateral torsional buckling

To show that the scheme is not only limited to calculating cross-sectional properties for the linear elastic case or taking into account physical nonlinearities, this example considers cross-sectional deformation by using geometric nonlinearity on the mesoscopic and macroscopic scale. The impact of this nonlinearity is shown by calculating a stability problem that is due to lateral torsional buckling. It is necessary to mention that the underlying beam theory leads to the basic 6 degrees of freedom per node and, thus, does not contain any assumption regarding the continuity of the cross-sectional warping between the elements. Therefore, it is expected that the scheme recognizes the correct maximum load level only for a limited set of examples and underesti-

Fig. 22 Normalized cross-section parameters of the U-shaped profile using DBC

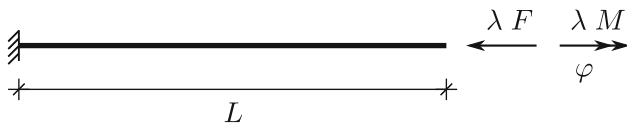
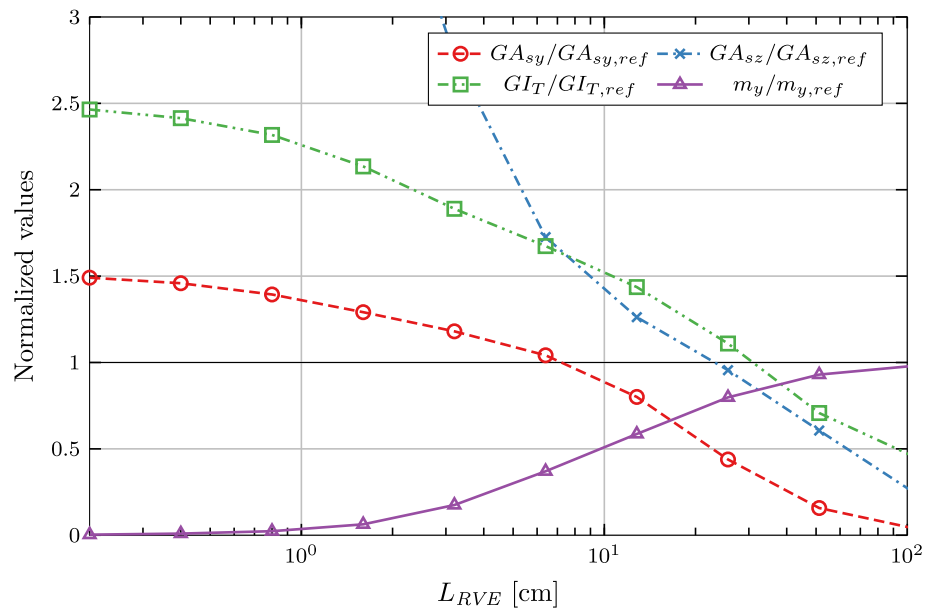


Fig. 23 Geometry and load of the system to investigate lateral torsional buckling

mates the maximum load level as soon as warping constraints or warping continuity play a significant role.

For the reasons mentioned above, the system is chosen according to Fig. 23. Its length has a value of $L = 150$ cm, and it is loaded with λF and λM . The values of the force and moment are $F = 100$ kN and $M = 0.1$ kN cm. Both applied loads are scaled with the load-factor λ . The applied moment M represents an imperfection only and is removed as soon as the system buckled.

Regarding the finite element mesh, 20 beam elements are employed on the macroscopic scale. For the mesoscopic scale, the cross-section described in the previous section is used. This time the mesh parameters are $n_c = 2$ and $n_w = 4$. In the length direction 3 elements are used for the PBCC and 5 elements for the DBC. In both cases, the length of the RVE is chosen as $L_{RVE} = 10$ cm. Furthermore, a reference solution is calculated using 3D brick elements with the same mesh parameters for the cross-section and 40 elements along the length of the system. To reduce the impact of the continuity of warping deformation, the boundary conditions are imposed with a constant traction interface element comparable to that in Sect. 4.1.

The results are depicted in Fig. 24. In this diagram, the unloading path is shown after the moment M was removed. Both the multiscale calculation with PBCC and the 3D model

(Ref.) yield nearly the same results. Looking at the DBC, no sign of instability can be observed. This is because the warping displacement is suppressed on the mesoscopic scale. For further comparison, analytical values of the critical loads are computed according to [18]. They evaluate to $\lambda_{TB} = 5.89$ in the case of lateral torsional buckling, $\lambda_{Bw} = 6.55$ for the first Euler case with respect to the weak axis, and $\lambda_{Bs} = 11.27$ for the first Euler case with respect to the strong axis. Even though all loads are applied at the center of gravity of the cross-section, they do not lead to a sufficient imperfection with DBC, and neither the Euler buckling case connected to the weak axis nor the one connected to the strong axis is triggered, but the equation system has negative diagonal elements after reaching the critical load of the first Euler buckling case.

5.3 Layered cross-section

Here, a layered cross-section is considered. The geometry of the cross-section is depicted in Fig. 25. Its width is b , and its height $h = 2h_L + h_C$. Furthermore, the core fraction ρ_C that describes the ratio between the layer height h_L and the core height h_C as $h_C = \rho_C h$ and $h_L = (1 - \rho_C)h/2$ is assumed. Regarding the material parameters, the factor α is introduced to describe the ratio between the stiffness of the core and the layers as $\alpha = E_C/E_L$. The value E_C is the Young’s modulus of the core and E_L the one of the face layers.

5.3.1 Effective properties

Here, the width is $b = 20$ cm, and the total height $h = 2h_L + h_C = 20$ cm. The focus lies in the evaluation of the tension stiffness EA , the bending stiffness EI_y with respect to the

Fig. 24 Load-factor λ versus tip-rotation φ

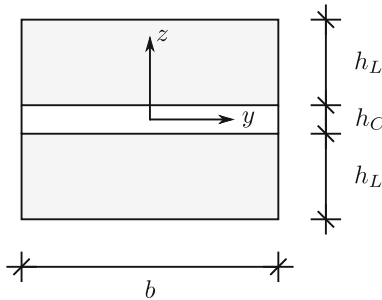
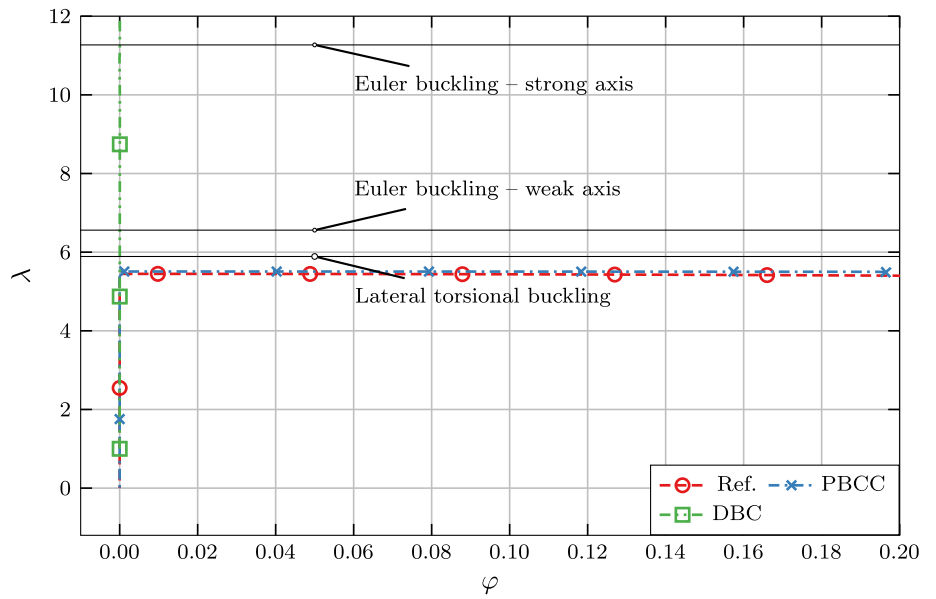


Fig. 25 Geometry of the layered cross-section

y-axis and the shear stiffness in the z-direction. The Young's modulus of the layer is chosen as $E_L = 1000 \text{ kN cm}^{-2}$, and the Poisson's ratio is assumed to be equal in the layer and the core, with a value of $\nu = 0.3$. For this cross-section, the analytical values for the tension and bending stiffness can be evaluated as

$$EA = E_L b (\alpha h_C + h_L)$$

$$EI_y = E_L b \left(\alpha \frac{h_C^3}{12} + 2 \left[\frac{h_L^3}{12} + s_L^2 h_L \right] \right). \quad (67)$$

For the shear correction factor, a solution for κ_z can be found in [25] and is evaluated with

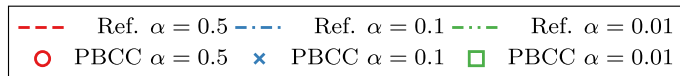
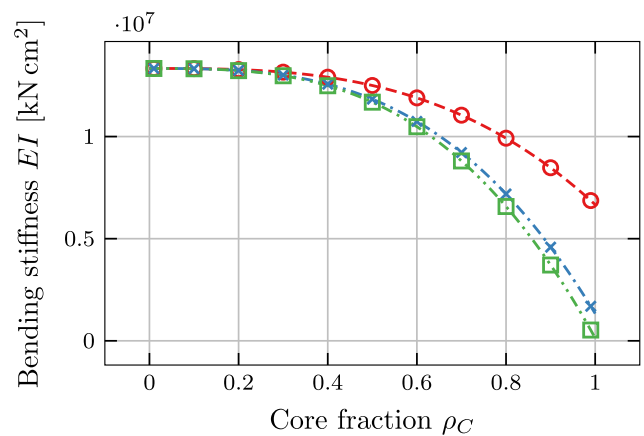
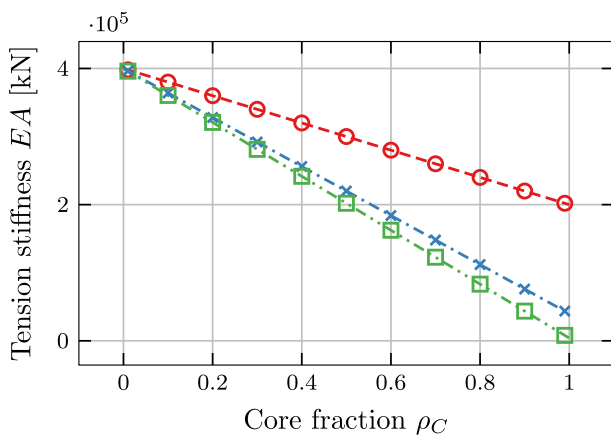


Fig. 26 Comparison of the resulting bending and tension stiffness for varying stiffness ratios α and core fractions ρ_C —layered cross-section

Fig. 27 Comparison between the analytically and numerically evaluated shear correction factor κ for varying stiffness ratios α and core fractions ρ_C —layered cross-section

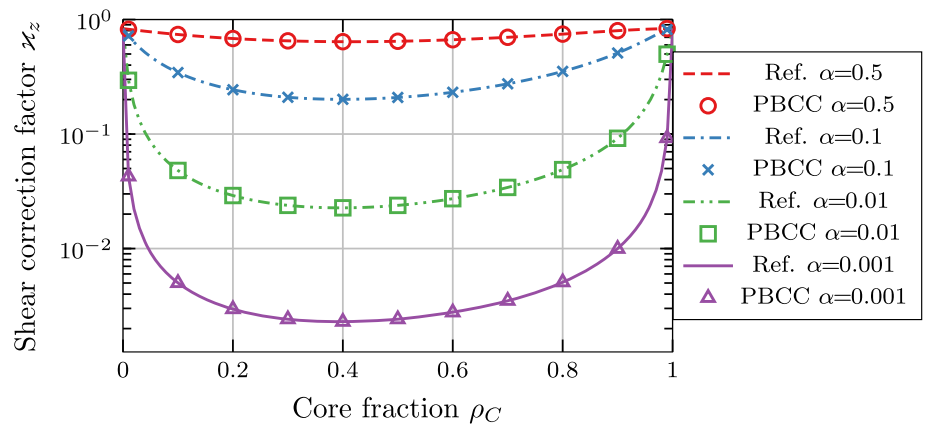
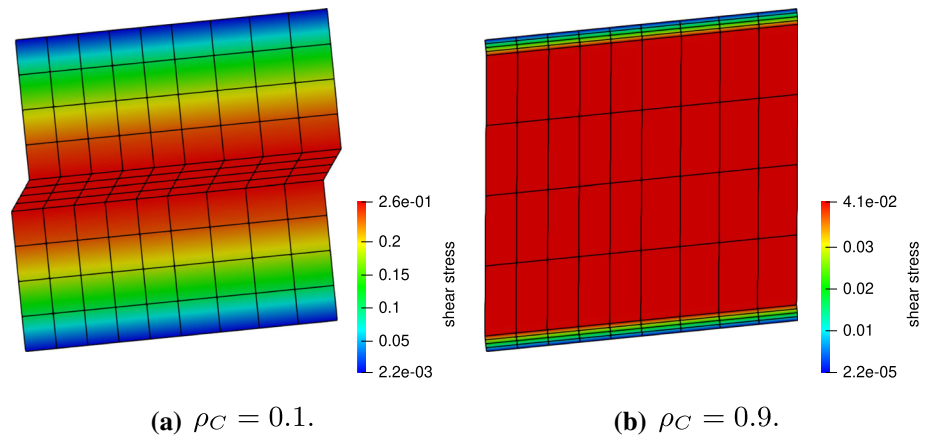


Fig. 28 Shear stresses and deformation of the RVE $\alpha = 0.001$ and $\gamma_z = 0.1$ in (kN cm^{-2})—layered cross-section



$$\begin{aligned}
 A(\rho_C) &= \frac{(1 - \rho_C)^3}{15} (3\rho_C^2 + 9\rho_C + 8), \\
 T_1(\rho_C) &= (1 - \rho_C^3) + \rho_C^3\alpha, \\
 T_2(\rho_C) &= \frac{1 - \rho_C}{\alpha} + \rho_C, \\
 T_3(\rho_C) &= (1 - \rho_C^2)^2 + \frac{8}{15}\alpha^2\rho_C^4 + \frac{4}{3}\alpha\rho_C^2(1 - \rho_C^2), \\
 T_4(\rho_C) &= A(\rho_C)\alpha + \rho_C T_3
 \end{aligned} \tag{68}$$

as

$$\kappa_z = \frac{4}{9} \frac{T_1^2}{T_2 T_4} \tag{69}$$

To compare the reference solutions Eqs. (67) and (69) with the results of the homogenization scheme, PBCC are used. Each layer of the RVE is meshed with 4 elements in thickness, 4 elements in width and 9 elements in length.

The results of the homogenization scheme for the tension and bending stiffnesses are depicted in Fig. 26. A dashed line is used to represent the reference solution according to Eq. (67). The results of the numerical homogenization are marked with the corresponding symbols. For all stiffness ratios α and core fraction ρ_C , numerically exact values are

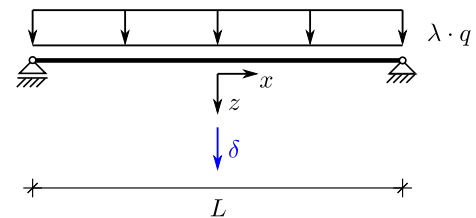


Fig. 29 Geometry of the macroscopic system

to be observed. This means that 7 digits agree, which is the used output precision.

Next, the shear correction factor is evaluated. Results are presented in Fig. 27. Again, the dashed lines represent the analytical solution and the results of the homogenization scheme are depicted with symbols. As before, the numerical results agree very well with the analytical solution Eq. (69). In the case of $\rho_C = 0$ and $\rho_C = 1$, the shear correction factor is $\kappa = 5/6$. In this case a homogeneous cross-section is evaluated. To name an extreme value, for $\alpha = 0.001$ and $\rho_C = 0.4$, the shear correction even drops to a value of $\kappa \approx 1/500$. The values are also compared with the results of the element according to [10], which leads to the same values.

To get insight into the shear deformation of the RVE, it is depicted for a core fraction of $\rho_C = 0.1$ in Fig. 28a and

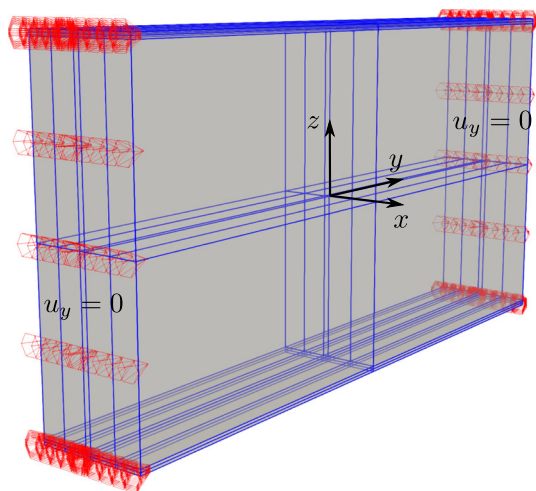


Fig. 30 Additional constraints to achieve a plate strip behavior

for a core fraction of $\rho_C = 0.9$ in Fig. 28b. In Fig. 28a, it is clearly visible that the shear strain is concentrated in the core, and the RVE shows noticeable warping. In contrast, warping deformation is less noticeable in Fig. 28b. One can see that the shear stresses are nearly constant within the core.

5.3.2 Plastic behavior

In this section, the behavior of the cross-section due to plasticization of the face layers is investigated. The example is taken from [13]. A linear elastic material behavior for the core is assumed with a Youngs’ modulus of $E = 70 \text{ N mm}^{-2}$ and a Poisson’s ratio of $\nu = 0.3$. For the face layers, a plastic behavior is assumed with $E_L = 70,000 \text{ N mm}^{-2}$, $\nu_L = 0.3$,

a yield stress of $Y_0 = 100 \text{ N mm}^{-2}$ and a hardening modulus of $H = 1000 \text{ N mm}^{-2}$. The geometry parameters are $h_C = 30 \text{ mm}$, $h_L = 0.5 \text{ mm}$ and $b = 60 \text{ mm}$.

The macroscopic system is depicted in Fig. 29. Its length is chosen as $L = 2000 \text{ mm}$, and it is loaded with $q = \lambda \cdot 0.06 \text{ N mm}^{-1}$. To represent the structure, 14 beam elements are used. Later, the displayed deflection δ versus the load factor λ is observed.

As the reference solution of [13] is for a plate strip and is not directly comparable with beam kinematics, additional constraints for the RVE are needed. They are depicted in Fig. 30. Here, the displacements u_y on opposite sides in the y -direction of the RVE are constraint. Due to those constraints, an equivalent behavior of the system can be achieved. Furthermore, the mesh of the RVE can be seen in Fig. 30. It has a length of $L_{RVE} = 10 \text{ mm}$, consists of 2 elements in width, 2 elements in height per layer and 5 elements in length. The interface element in the center of the RVE has a thickness of $d = 0.5 \text{ mm}$. The results of the computation are presented in Fig. 31. For comparison, the calculation is performed with the basic PBCC (PBCCb). As expected, the solution of the system is too soft, as it is calculated using the beam assumptions. Using PBCC with the additional constraints given in Fig. 30, the plate strip behavior can be simulated with the multiscale approach. Under those assumptions, it is possible to reproduce the reference solution (Ref.).

5.4 Structural homogenization: right angle bent

The last example considers an internal structure that will be homogenized. It is intended to show that the scheme’s capabilities go beyond the modeling of cross-sections only.

Fig. 31 Load deflection behavior of the system

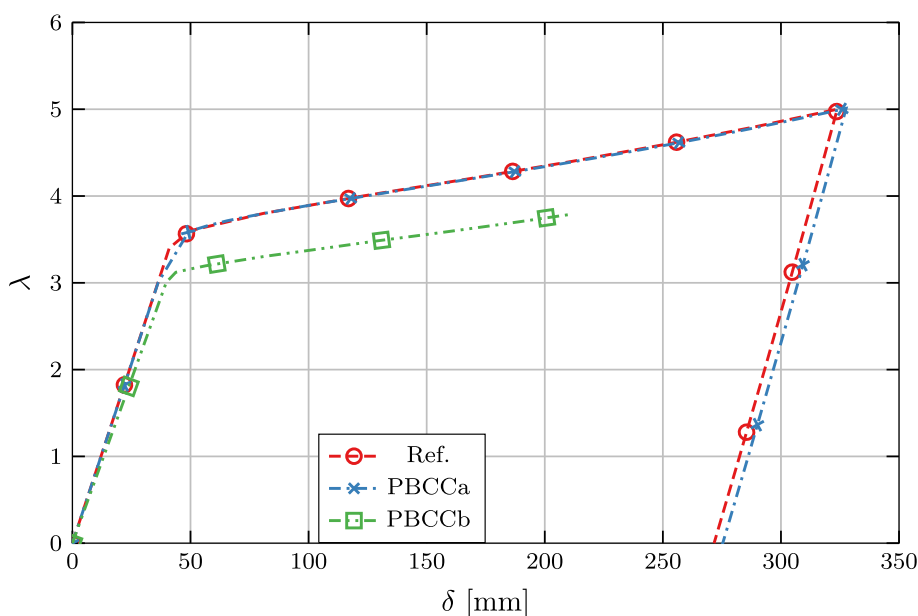
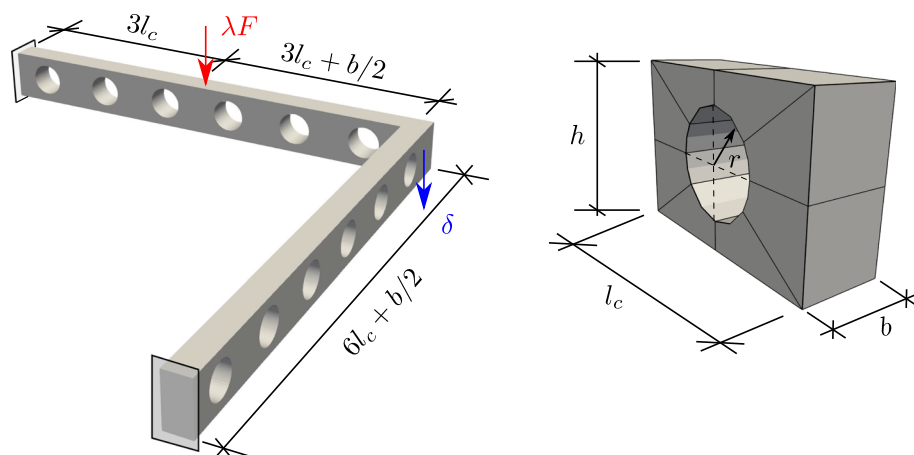


Fig. 32 Geometry and loading of the right angle and its local structure



The geometry of the model and its internal structure is depicted in Fig. 32. With length $l_c = 30$ cm, width $b = 10$ cm, height $h = 20$ cm and radius $r = 6.5$ cm, the structure is completely defined. It is worth mentioning that the hole with a radius of $r = 6.5$ cm reduces the cross-section by 65 %. Therefore, the kinematical assumptions of the beam theory are no longer valid in every point of the structure. But it will be shown, that the proposed scheme can reproduce the structural behavior. Furthermore, geometrical and physical nonlinearity is included on both scales. Regarding the latter, a linear elastic, ideal plastic material behavior with a Young's modulus $E = 21,000$ kN cm⁻², a Poisson's ratio of $\nu = 0.3$ and a yield stress of $Y_0 = 23.5$ kN cm⁻² is chosen. The structure is loaded by a force $F = \lambda \cdot 50$ [kN], whereby λ is the load factor. Furthermore, both ends are clamped. Due to the given geometry and loading, the system is subjected to bending, shearing and torsion.

To describe the mesh, the internal structure in Fig. 32 is subdivided into 8 blocks. Each of these blocks is meshed by $4 \times 4 \times 4$ elements. The resulting mesh for the RVE with PBCC is depicted in Fig. 33. Here, two internal structures are used to represent the RVE. In the center of the RVE, the interface element is added. Its thickness is chosen as $d = 0.125(l_c/2 - r) = 1.0625$ cm. Two of the internal structures are used because the interface element is designed to be applied in the center of the RVE, and its kinematical assumptions are based on beam kinematics. Therefore, it is necessary to construct a part of the mesh in the center of the RVE in which these assumptions are valid. Regarding the macroscopic beam mesh, 6 linear beam elements per arm are chosen. Consequently, the integration points of these elements approximately coincide with the centers of the holes. For comparison, the structure is evaluated using 3D brick elements with the same mesh parameters as described above.

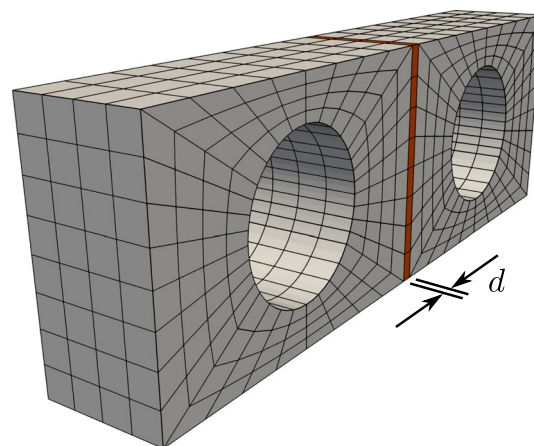


Fig. 33 Mesh of the RVE for PBCC including the interface element of thickness d

The results of the calculation are depicted in Fig. 34. As shown, the calculated load deflection behavior of the multi-scale model (PBCC) is in good agreement with the 3D model (Ref.).

The equivalent plastic strains at $\delta = 2.1$ cm and $\lambda = 7.4$ are shown in Fig. 35. As expected, plasticity occurs at the weakest position with the highest load near the clamping. To get further insight into the stress state, a coordinate system to identify the stresses is included.

Finally, the stresses along a line are plotted in Fig. 36. The line is parallel to the height direction and is tangent to the hole of the internal structure at 8.5 cm from the clamping. In addition, it is located at the center of the internal structures' width direction. Stresses are evaluated in a plastic state with a corner displacement of $\delta = 2.1$ cm and a load factor of $\lambda = 7.4$. The results of the multiscale model agree very well with those of the reference solution.

Fig. 34 Load deflection behavior of the right angle—load factor λ versus corner displacement δ

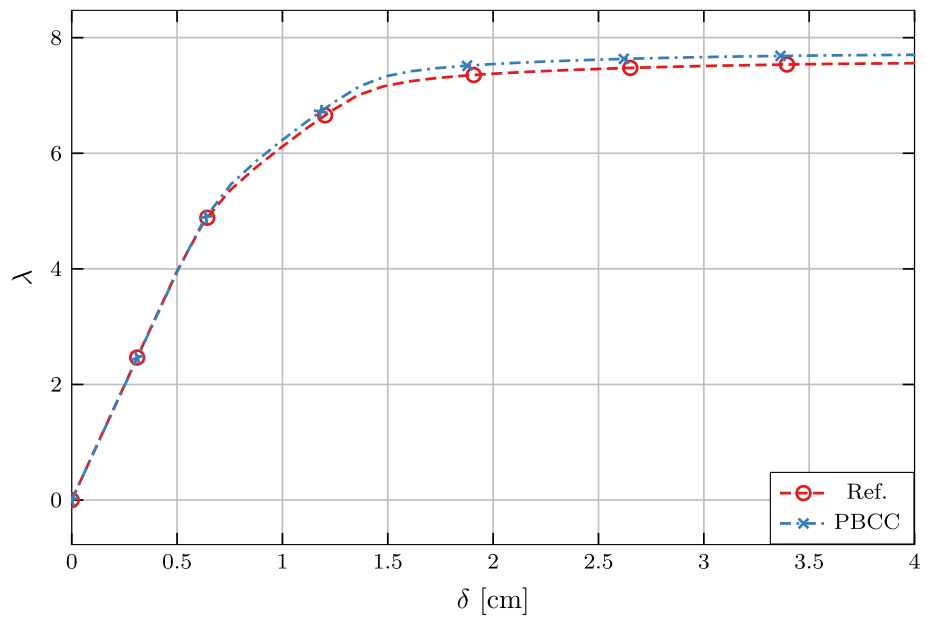
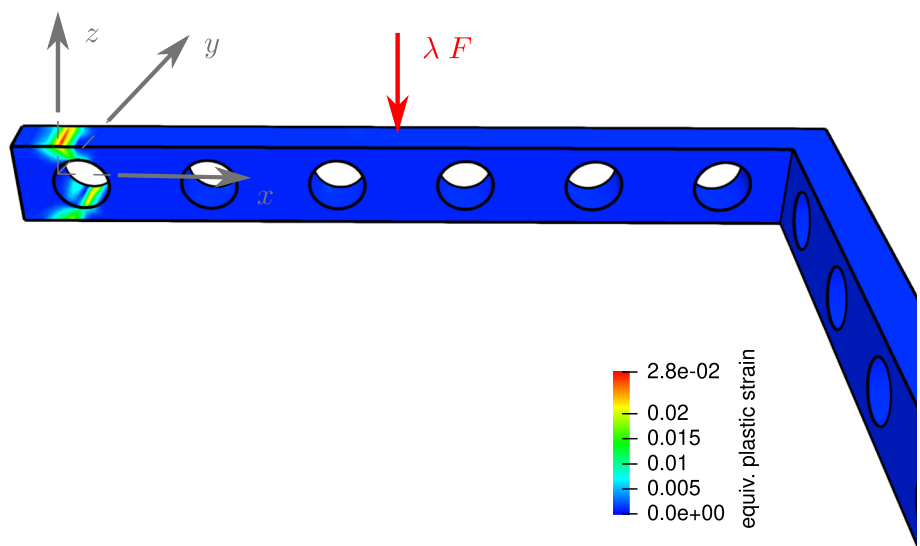


Fig. 35 Equivalent plastic strains of the 3D brick model at $\delta = 2.1$ cm and $\lambda = 7.4$



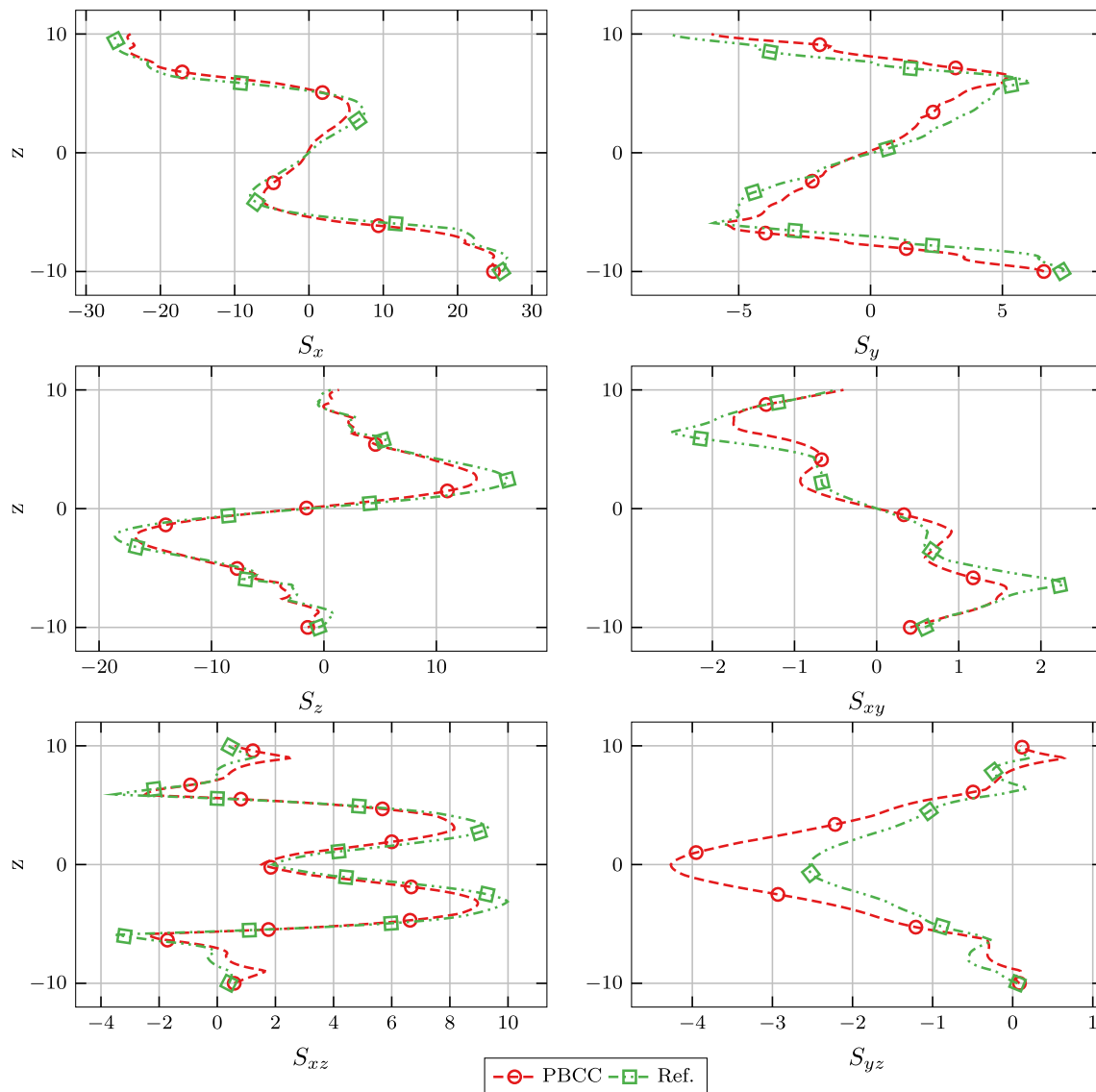


Fig. 36 Stresses through height at 8.5 cm from the clamping of the loaded arm in (kN cm^{-2})— $\delta = 2.1$ cm and $\lambda = 7.4$

6 Conclusion

In this contribution, a multiscale model for beam elements is proposed. The theory itself is based on a first-order homogenization scheme. It is shown that the direct application of the scheme using the beam kinematics leads to length-dependent results for the homogenized shear stiffnesses. The source of the length dependencies is identified and is connected to the moment balance. Additional constraints are proposed that remove this length dependency. As a result, the scheme is able to reproduce well-known cross-sectional values of simple homogeneous cross-sections and layered cross-sections. Furthermore, the model allows for the consideration of physical nonlinearity such as plasticity. Alongside the calculation of effective cross-sectional prop-

erties using the undeformed geometry, the scheme allows the consideration of cross-sectional deformations by employing geometrical nonlinearity on the mesoscale. This fact allows the discovery of possible stability problems like lateral torsional buckling. As a 3D RVE is homogenized, the scheme's capabilities reach beyond pure cross-section modeling and allow the consideration of periodic structures along the length direction.

References

1. Buannic N, Cartraud P (2001) Higher-order effective modeling of periodic heterogeneous beams. II. Derivation of the proper boundary conditions for the interior asymptotic solution. *Int J Solids Struct* 38(40–41):7163–7180

2. Carrera E, Giunta G, Nali P, Petrolo M (2010) Refined beam elements with arbitrary cross-section geometries. *Comput Struct* 88(5–6):283–293
3. Cartraud P, Messenger T (2006) Computational homogenization of periodic beam-like structures. *Int J Solids Struct* 43(3):686–696
4. Coenen EWC, Kouznetsova VG, Geers MGD (2010) Computational homogenization for heterogeneous thin sheets. *Int J Numer Methods Eng* 83(8–9):1180–1205
5. Feyel F (1998) Application du calcul parallèle aux modèles á grand nombre de variables internes, PhD Thesis. ONERA
6. Feyel F, Chaboche JL (2000) FE2 multiscale approach for modelling the elastoviscoplastic behaviour of long fibre SiC/Ti composite materials. *Comput Methods Appl Mech Eng* 183(3–4):309–330
7. Geers MGD, Coenen EWC, Kouznetsova VG (2007) Multi-scale computational homogenization of structured thin sheets. *Model Simul Mater Sci Eng* 15(4):S393–S404
8. Gruttmann F, Wagner W (2001) Shear correction factors in Timoshenko's beam theory for arbitrary shaped cross-sections. *Comput Mech* 27(3):199–207
9. Gruttmann F, Wagner W (2013) A coupled two-scale shell model with applications to layered structures. *Int J Numer Methods Eng* 94(13):1233–1254
10. Gruttmann F, Wagner W (2017) Shear correction factors for layered plates and shells. *Comput Mech* 59(1):129–146
11. Gruttmann F, Sauer R, Wagner W (1998) A geometrical nonlinear eccentric 3D-beam element with arbitrary cross-sections. *Comput Methods Appl Mech Eng* 160(3–4):383–400
12. Gruttmann F, Wagner W, Sauer R (1998) Zur Berechnung von Wölbfunktion und Torsionskennwerten beliebiger Stabquerschnitte mit der Methode der finiten Elemente. *Bauingenieur* 73:138–143
13. Gruttmann F, Knust G, Wagner W (2017) Theory and numerics of layered shells with variationally embedded interlaminar stresses. *Comput Methods Appl Mech Eng* 326:713–738
14. Heller D, Gruttmann F (2016) Nonlinear two-scale shell modeling of sandwiches with a comb-like core. *Compos Struct* 144:147–155
15. Hill R (1952) The elastic behaviour of a crystalline aggregate. *Proc Phys Soc London Sect A* 65(5):349–354
16. Hodges DH (2006) Nonlinear composite beam theory, vol 213. *Progress in astronautics and aeronautics*. American Institute of Aeronautics and Astronautics, Reston
17. Klinkel S, Govindjee S (2002) Using finite strain 3D-material models in beam and shell elements. *Eng Comput* 19(3):254–271
18. Kollbrunner CF, Meister M (1961) *Knicken, Biegedrillknicken, Kippen*. Springer, Berlin
19. Marković D, Ibrahimbegović A (2004) On micro-macro interface conditions for micro scale based fem for inelastic behavior of heterogeneous materials. *Comput Methods Appl Mech Eng* 193(48–51):5503–5523
20. Saeb S, Steinmann P, Javili A (2016) Aspects of computational homogenization at finite deformations: a unifying review from Reuss' to Voigt's bound. *Appl Mech Rev* 68(5):050801
21. Sayyad AS (2011) Comparison of various refined beam theories for the bending and free vibration analysis of thick beams. *Appl Comput Mech* 5:217–230
22. Schröder J (2000) *Homogenisierungsmethoden der nichtlinearen Kontinuumsmechanik unter Beachtung von Stabilitätsproblemen*. Habilitation, Bericht Nr I-7 aus dem Institut für Mechanik (Bauwesen), Universität Stuttgart
23. Simo JC, Vu-Quoc L (1991) A geometrically-exact rod model incorporating shear and torsion-warping deformation. *Int J Solids Struct* 27(3):371–393
24. Timoshenko SP, Goodier JN (1951) *Theory of elasticity*. McGraw-Hill, New York
25. Vlachoutsis S (1992) Shear correction factors for plates and shells. *Int J Numer Methods Eng* 33(7):1537–1552
26. Wackerfuß J, Gruttmann F (2009) A mixed hybrid finite beam element with an interface to arbitrary three-dimensional material models. *Comput Methods Appl Mech Eng* 198(27):2053–2066
27. Wackerfuß J, Gruttmann F (2011) A nonlinear Hu-Washizu variational formulation and related finite-element implementation for spatial beams with arbitrary moderate thick cross-sections. *Comput Methods Appl Mech Eng* 200(17–20):1671–1690
28. Wagner W, Gruttmann F (2001) Finite element analysis of Saint-Venant torsion problem with exact integration of the elastic-plastic constitutive equations. *Comput Methods Appl Mech Eng* 190(29–30):3831–3848
29. Wagner W, Gruttmann F (2013) A consistently linearized multi-scale model for shell structures. In: Pietraszkiewicz W (ed) *Shell structures*. CRC Press, Boca Raton
30. Xu L, Cheng G, Yi S (2016) A new method of shear stiffness prediction of periodic Timoshenko beams. *Mech Adv Mater Struct* 23(6):670–680
31. Yu W, Hodges DH (2005) Generalized Timoshenko theory of the variational asymptotic beam sectional analysis. *J Am Helicopter Soc* 50(1):46–55

Publisher's Note Springer Nature remains neutral with regard to jurisdictional claims in published maps and institutional affiliations.